

TECHNICAL REPORT STANDARD PAGE

- | | |
|--|---|
| 1. Title and Subtitle
Exploration of Drone and Remote Sensing Technologies
in Highway Embankment Monitoring and Management
(Phase I) | 5. Report No.
FHWA/LA.23/690 |
| 2. Author(s)
Zhongjie Zhang, Ph.D., P.E., Qiming Chen, Ph.D., P.E. | 6. Report Date
November 2023 |
| 3. Performing Organization Name and Address
Louisiana Transportation Research Center
4101 Gourrier Avenue
Baton Rouge, LA 70808 | 7. Performing Organization Code
LTRC Project Number: 18-1P
SIO Number: DOTLT1000216 |
| 4. Sponsoring Agency Name and Address
Louisiana Department of Transportation and Development
P.O. Box 94245
Baton Rouge, LA 70804-9245 | 8. Type of Report and Period Covered
Final Report
08/17-08/2023 |
| | 9. No. of Pages
107 |

10. Supplementary Notes

Conducted in Cooperation with the U.S. Department of Transportation, Federal Highway Administration

11. Distribution Statement

Unrestricted. This document is available through the National Technical Information Service, Springfield, VA 21161.

12. Key Words

Remote Sensing, Thermal Camera, Multispectral Camera, Drone, Embankment, Dam, Soil Moisture

13. Abstract

Monitoring the spatial-temporal variation of surface moisture content in highway soil embankment/dam has a practical implication for earth embankment/dam safety. The knowledge of soil moisture content on the surface of earth embankment/dams can help engineers monitor the dynamic evolution of slope stability due to the adverse effect of excessive moisture and seepage, thus evaluating the risk of stability failure. Nevertheless, traditional inspections on the ground by trained engineers and technicians are laborious, time consuming, and costly. Recent advancements in commercial remote sensing technologies (microwave, thermal infrared, and optical), however, provide opportunities to obtain precise measurements of displacements as well as surface moisture conditions from soil embankments/dams in a cost-effective manner. This research has explored the capabilities of drone-mounted remote sensing sensors for soil moisture detection on embankment/dam soils. Two specific remote sensors were evaluated in this study: FLIR Vue Pro R, a radiometric thermal camera, and MicaSense RedEdge, a multispectral camera for precision agriculture. They were evaluated both in laboratory and field settings on embankment/dam soils for their accuracy, repeatability, and dependability. The laboratory tests showed that the decreasing trend of measured apparent temperature is obvious when the moisture content is low. After that, the relationship curve flattens out. Meanwhile, the field results showed that the drier the soil, the higher the measured apparent temperature. The correlation between the soil moisture content and apparent temperature reading from the thermal camera is very complicated and only has a relative value for comparison purpose when the ambient environment is not considered. For the multispectral camera, the drier the soil, the higher the pixel values for all five bands. No clear trend was observed between Normalized Difference Vegetation Index (NDVI)/Green Normalized Difference Vegetation Index (GNDVI) and soil moisture. The index combining land surface temperature and vegetation within the NDVI/Land Surface Temperature (LST) space showed promising results in this study. The findings of this study prove that the thermal camera is capable of distinguishing different moisture zones and therefore a promising tool for rapid mapping of earth embankment and dam slope surface moisture conditions for potential stability risk to supplement traditional ground inspections.

Project Review Committee

Each research project will have an advisory committee appointed by the LTRC Director. The Project Review Committee is responsible for assisting the LTRC Administrator or Manager in the development of acceptable research problem statements, requests for proposals, review of research proposals, oversight of approved research projects, and implementation of findings.

LTRC appreciates the dedication of the following Project Review Committee Members in guiding this research study to fruition.

LTRC Administrator/Manager

Zhongjie Zhang

Pavement and Geotechnical Research Administrator

Members

Jesse Rauser

Miranda Perkins

James Chatagnier

Francisco Gudiel

Stanley Ard

Brenda Browning

Dustin Smith

Josh Duplantis

James Mitchell

Li Yang

Timothy Harper

Directorate Implementation Sponsor

Christopher P. Knotts, P.E.

DOTD Chief Engineer

Exploration of Drone and Remote Sensing Technologies in Highway Embankment Monitoring and Management (Phase I)

By

Zhongjie Zhang, Ph.D., P.E.

Qiming Chen, Ph.D., P.E.

Louisiana Transportation Research Center
4101 Gourrier Avenue
Baton Rouge, LA 70808

LTRC Project No. 18-1P
SIO No. DOTLT1000216

conducted for

Louisiana Department of Transportation and Development
Louisiana Transportation Research Center

The contents of this report reflect the views of the author/principal investigator who is responsible for the facts and the accuracy of the data presented herein.

The contents do not necessarily reflect the views or policies of the Louisiana Department of Transportation and Development, the Federal Highway Administration or the Louisiana Transportation Research Center. This report does not constitute a standard, specification, or regulation.

November 2023

Abstract

Monitoring the spatial-temporal variation of surface moisture content in highway soil embankment/dam has a practical implication for earth embankment/dam safety. The knowledge of soil moisture content on the surface of earth embankment/dams can help engineers monitor the dynamic evolution of slope stability due to the adverse effect of excessive moisture and seepage, thus evaluating the risk of stability failure. Nevertheless, traditional inspections on the ground by trained engineers and technicians are laborious, time consuming, and costly. Recent advancements in commercial remote sensing technologies (microwave, thermal infrared, and optical), however, provide opportunities to obtain precise measurements of displacements as well as surface moisture conditions from soil embankments/dams in a cost-effective manner.

This research has explored the capabilities of drone-mounted remote sensing sensors for soil moisture detection on embankment/dam soils. Two specific remote sensors were evaluated in this study: FLIR Vue Pro R, a radiometric thermal camera, and MicaSense RedEdge, a multispectral camera for precision agriculture. They were evaluated both in laboratory and field settings on embankment/dam soils for their accuracy, repeatability, and dependability. The laboratory tests showed that the decreasing trend of measured apparent temperature is obvious when the moisture content is low. After that, the relationship curve flattens out. Meanwhile, the field results showed that the drier the soil, the higher the measured apparent temperature. The correlation between the soil moisture content and apparent temperature reading from the thermal camera is very complicated and only has a relative value for comparison purpose when the ambient environment is not considered. For the multispectral camera, the drier the soil, the higher the pixel values for all five bands. No clear trend was observed between Normalized Difference Vegetation Index (NDVI)/Green Normalized Difference Vegetation Index (GNDVI) and soil moisture. The index combining land surface temperature and vegetation within the NDVI/Land Surface Temperature (LST) space showed promising results in this study. The findings of this study prove that the thermal camera is capable of distinguishing different moisture zones and therefore a promising tool for rapid mapping of earth embankment and dam slope surface moisture conditions for potential stability risk to supplement traditional ground inspections.

Acknowledgments

This research project was funded by the Louisiana Department of Transportation and Development (DOTD) and the Louisiana Transportation Research Center. The authors would like to thank Josh Duplantis and DOTD Aviation section for their assistance during field testing. Thanks should also be given to James Mitchell and DOTD OTS GIS group for their assistance on software issues. The contributions of Terrell Gorham, Benjamin Key, and Biyuan Zheng are also noteworthy.

Implementation Statement

The results of this study demonstrate the capability of the drone-mounted thermal camera to qualitatively distinguish different moisture zones, which can help identify potential problematic locations in an earth embankment or dam, based on the following facts:

1. Thermal image contrast (i.e., relative differences in surface temperature), instead of actual land surface temperature, is more critical. In other words, as long as there was moisture contrast, the image should be sufficient for detecting areas with abnormal soil moisture conditions.
2. At short range, the uncertainty in the measurement due to the atmospheric absorption and its emission is minimum.
3. The drone-mounted thermal camera acquires images in a relatively short time for each flight with a consistent environmental condition. In other words, even if there is environmental influence, the influence from the environment should be nearly the same across the images in each pixel.

The authors of this report therefore recommend that DOTD start to adopt drone-based infrared thermography technology in highway embankment and dam inspections. It will benefit DOTD with a number of advantages, including rapid mapping of earth embankment or dam slope surface moisture conditions without any left out location/area due to difficult-to-reach; fast processing all the collected data using computers to identify the potential problematic locations before any field failure occurs; and developing a system-wide warning system for DOTD.

Table of Contents

Technical Report Standard Page	1
Project Review Committee	2
LTRC Administrator/Manager	2
Members	2
Directorate Implementation Sponsor	2
Exploration of Drone and Remote Sensing Technologies in Highway Embankment	
Monitoring and Management (Phase I)	3
Abstract	4
Acknowledgments.....	5
Implementation Statement	6
Table of Contents	7
List of Tables.....	9
List of Figures.....	10
Introduction.....	12
Literature Review.....	15
Microwave Remote Sensing	15
Thermal Infrared Remote Sensing.....	17
Optical Remote Sensing.....	22
Objective.....	27
Scope.....	28
Methodology.....	29
Drone-Mounted Remote Sensing Sensors	29
Laboratory Testing	34
Field Testing at Pavement Research Facility Site.....	35
Field Testing at I-10 @ LA30 Embankment Site.....	37
Field Testing at Iatt Lake Dam Site	39
Field Testing at Vernon Lake Dam Site	40
Discussion of Results.....	42
Laboratory Testing	42
Field Testing at Pavement Research Facility Site.....	51
Field Testing at I-10 @ LA30 Embankment Site.....	68
Field Testing at Iatt Lake Dam Site	82
Field Testing at Vernon Lake Dam Site	92
Conclusions.....	95

Recommendations.....	96
Acronyms, Abbreviations, and Symbols.....	97
References.....	99

List of Tables

Table 1. Microwave frequency bands	16
Table 2. FLIR Vue Pro R thermal camera specifications.....	29
Table 3. RedEdge TM multispectral camera specifications.....	33
Table 4. Spectral bands of RedEdge TM multispectral camera.....	34
Table 5. Temperature readings at different heights.....	42

List of Figures

Figure 1. Cracks due to shrinkage of clayey soils along the side of highway embankment	13
Figure 2. Slope failures at I-10 @ Bluebonnet	14
Figure 3. Example of soil moisture storage (6 in. capacity) [4]	14
Figure 4. Spectral intensity of blackbody radiation	18
Figure 5. Spectral intensity of blackbody radiation at temperature of the Earth	18
Figure 6. VIT trapezoid [42]	20
Figure 7. A Conceptual LST-NDVI triangle [44]	21
Figure 8. Measured spectra of a soil sample with different soil moisture [54].....	23
Figure 9. Simulated spectra of plant leaves with different equivalent water thickness (EWT) levels [59]	23
Figure 10. Principle of a thermal camera detecting infrared radiation from soil.....	31
Figure 11. Effect of thermal inertia on diurnal soil surface temperature variation.....	32
Figure 12. Principle of a multispectral camera detecting radiation reflected by soil	34
Figure 13. Laboratory testing setup	35
Figure 14. Drone flight testing site at PRF	36
Figure 15. A typical flight path at PRF site.....	37
Figure 16. Aerial view of I-10 @ LA30 embankment site	38
Figure 17. A close view of sliding failure area	38
Figure 18. Flight paths for I-10 @ LA30 embankment site	39
Figure 19. Aerial view of Iatt Lake Dam	40
Figure 20. Flight path for Iatt Lake Dam.....	40
Figure 21. Aerial view of Vernon Lake Dam	41
Figure 22. Flight paths for Vernon Lake Dam	41
Figure 23. Examination of camera warmup time.....	43
Figure 24. Examination of camera battery change effect	43
Figure 25. Apparent temperature vs moisture content	45
Figure 26. Measured temperature vs. emissivity	46
Figure 27. Picture and thermal image of soil samples	47
Figure 28. Test setup with cardboard box	49
Figure 29. Apparent temperature vs moisture content with new test setup	50
Figure 30. Impact of the soil below the surface on measured apparent temperatures	50
Figure 31. Embankment soil with different moisture contents during flight session 3	51
Figure 32. Embankment soil with different moisture contents during flight session 4	52
Figure 33. Embankment soil with different moisture contents during flight session 5	52

Figure 34. Thermal image of embankment soil slope taken from ground.....	53
Figure 35. Thermal images of embankment soil slope at different heights.....	54
Figure 36. Variation of apparent soil surface temperature with moisture for flight session 355	
Figure 37. Variation of apparent soil surface temperature with moisture for flight session 455	
Figure 38. Variation of apparent soil surface temperature with moisture for flight session 556	
Figure 39. Interested area search	56
Figure 40. Manually stitched images	57
Figure 41. Geotagger by sUAS.....	58
Figure 42. Thermal map for PRF site	58
Figure 43. Orthomosaic map for PRF site	59
Figure 44. Raw image of individual band.....	60
Figure 45. Spectral profile for flight session 3	62
Figure 46. Spectral profile for flight session 4	64
Figure 47. Spectral profile for flight session 5	65
Figure 48. NDVI profile	66
Figure 49. GNDVI profile.....	67
Figure 50. Orthomosaic map for I-10 @ LA30 embankment.....	69
Figure 51. Raw image of individual band for I-10 @ LA30 embankment.....	70
Figure 52. Thermal image near the failure aArea for I-10 @ LA30 embankment.....	73
Figure 53. Apparent temperature profile across I-10 @ LA30 embankment near the failure area	73
Figure 54. Orthomosaic map near the failure area for I-10 @ LA30 embankment.....	74
Figure 55. NDVI profile across I-10 @ LA30 embankment near the failure area	74
Figure 56. Thermal image near the suspicious area for I-10 @ LA30 embankment.....	75
Figure 57. Apparent temperature profile across I-10 @ LA30 embankment near the suspicious area.....	75
Figure 58. Orthomosaic map near the suspicious area for I-10 @ LA30 embankment ...	75
Figure 59. NDVI profile across I-10 @ LA30 embankment near the suspicious area	76
Figure 60. Scatterplots of Surface temprature and NDVI.....	76
Figure 61. Thermal map of I-10 @ LA30 embankment	77
Figure 62. Orthomosaic map for Iatt Lake Dam.....	83
Figure 63. Raw image of individual band for Iatt Lake Dam.....	84
Figure 64. Thermal map for Iatt Lake Dam	89
Figure 65. Sliding area for Iatt Lake Dam	91
Figure 66. Thermal map for Vernon Lake Dam.....	93

Introduction

Louisiana highway embankments were sometimes built with high plasticity soils due to historical reasons. Over time, some embankments have experienced surface sliding failures, resulting in a safety issues and causing traffic disruptions. Since no warning system is available for this type of failure, the Louisiana Department of Transportation and Development (DOTD) can only respond to them after the fact with costly remediation. The reason for lacking a proactive highway embankment maintenance, management, and warning system is that the embankment system is extensive and assessing their condition using traditional site inspections by trained engineers and technicians is laborious, time-consuming, and costly.

Field observations have indicated that typical highway embankment failures encountered in Louisiana are related to the change of moisture content in embankment soils with high plasticity indices [1]. Usually, the sliding zone of a slope failure has much higher moisture contents than the adjacent intact zones. The extra moisture was not from the inner core of the embankment, but from surface intrusion outside of the embankment, most likely from the top portion of the slope of the embankment. The channels for this moisture intrusion can be shrinkage cracks formed at the slope surface in the dry seasons. Figure 1 shows an example of such cracks occurring along the slope of a highway embankment.

Figure 1. Cracks due to shrinkage of clayey soils along the side of highway embankment



A shallow surface failure usually involves three phases: shrinkage crack formation in the slope during dry seasons; infiltration of water into soil mass through cracks or fissures in subsequent wet seasons; and deterioration of shear strength of clayey soils to the extent that the shear forces within a slope cannot be adequately resisted, all of which contribute to a localized slope failure. How surface water infiltrates deep into a cohesive slope can be explained as follows. Newly built embankments should not have any cracks or fissures existing in the slope surfaces. When clayey soils with a high shrinkage/swell potential are exposed to dry and wet weather cycles, they will shrink and expand accordingly. This shrinking and expanding cycle causes fissures and cracks to develop in the slope surface, allowing surface water to enter, become trapped, and saturate the soils. As the cycle repeats, the fissures and cracks become wider and deeper until a slope failure takes place. During a prolonged wet season with a great deal of precipitation, the surface water will not only be trapped in these fissures and cracks, but also have enough time to soak the soil adjacent to these fissures and cracks. As the degree of soil saturation increases, their shear strength will dramatically decrease due to the interaction between the water and clay particles. As such, soils in slopes will lose their initial shear strength established during soil compaction at its optimum moisture content. This is the reason why most slope surface failures occur when its soils become totally saturated [2] [3].

It is worthwhile to point out that this kind of soil weakening process in an earth embankment is, based on field observation, very difficult (if not impossible) to predict. One such example is the

two slope failures that occurred at the intersection of interstate I-10 and Bluebonnet in Baton Rouge, Louisiana, as shown in Figure 2. The first slope slid in the year 2000 after serving approximately 20 years, but the second one occurred in about year 2020, approximately 20 years apart. Since these two slopes were built at the same location and with same material at the same time, it can be assumed that this kind of surface sliding is a random event. Therefore, the field observation of embankment soil surface moisture conditions becomes very important for evaluating their stability. Since the soils in a slope, before sliding, need to store enough moisture with a sustainable period of time, both of them together can be a good indicator of slope surface stability. Figure 3 shows an example of soil moisture storage in the central Louisiana. Soil moisture storage refers to the amount of water held in the soil at any particular time.

Figure 2. Slope failures at I-10 @ Bluebonnet

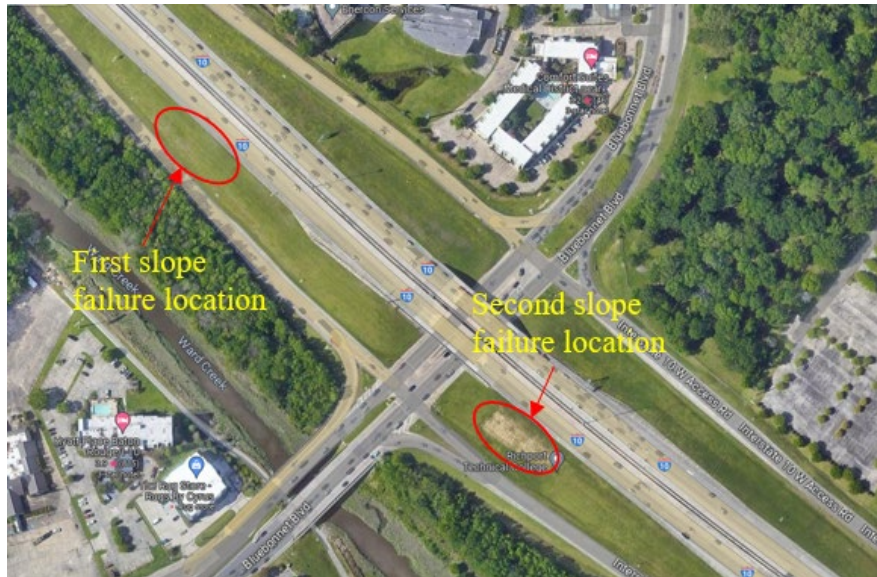
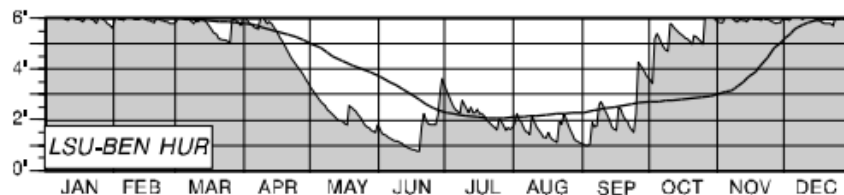


Figure 3. Example of soil moisture storage (6 in. capacity) [4]



Literature Review

It is well known that soil water content plays a vital role in various fields, such as civil engineering, hydrology, soil science, agriculture, meteorology, etc. Measuring soil moisture through remote sensing technology has been studied since 1970s [5] [6] [7] [8], mostly using the satellite as platform. Electromagnetic radiation emitted and reflected by the soil surface are two vital measurements when remote sensing technology is used. In recent years, research on using remote sensing techniques in detecting of soil moisture has made great progress [9]. Based on the spectrum range, remote sensing techniques that are mostly researched for surface soil moisture detection, are microwave remote sensing, thermal infrared remote sensing, and optical remote sensing.

Microwave Remote Sensing

The microwave region of the spectrum has a wavelength ranging from 1 mm to 1 m in wavelength, which corresponds to frequency from 300 GHz to 300 MHz. It is more common to refer to microwave in terms of frequency rather than wavelength. This range has been divided into several bands, each represented by a letter, as shown in Table 1 [10]. Microwave radiation can penetrate clouds, rain, and dust as the longer wavelengths are not susceptible to atmospheric scattering which affects shorter optical wavelengths. This property allows detection of microwave energy day and night in all weather conditions. Microwave remote sensing has been used for surface soil moisture detection since 1970s [5] [7] [8]. Microwave remote sensing includes both active and passive forms of remote sensing.

Passive microwave remote sensing uses the same principle as thermal infrared remote sensing. All objects emit microwave energy but much weaker than thermal infrared energy. Thus, a passive microwave sensor (radiometer or scanner), requires large field of view and wide bands to detect enough energy to record a signal. As such, passive microwave data has the characteristic of high temporal resolution and low spatial resolution. The emitted microwave energy is related to the temperature and emissivity of soil. The emissivity of soil depends on its dielectric constant, which is found to be strongly dependent on soil moisture content. The intensity of the emitted microwave energy is generally characterized by brightness temperature, the temperature of a blackbody that would emit the same amount of radiation as a grey body object.

Active microwave remote sensing provides its own source of microwave radiation to illuminate the soil and then detects the part that is backscattered by the soil. The intensity of the backscattered signal allows one to discriminate between different targets, while the two-way

travel time for the signal (transmission to reception) is used to determine the distance to the target. The moisture dependent dielectric constant of soil has a significant effect on the intensity of backscattered signal, which is characterized by backscattering coefficient.

Table 1. Microwave frequency bands

Letter Designation	Frequency Range	Wavelength
UHF	300-1000 MHz	30 cm to 100 cm
L band	1 to 2 GHz	15 cm to 30 cm
S band	2 to 4 GHz	7.5 cm to 15 cm
C band	4 to 8 GHz	3.75 cm to 7.5 cm
X band	8 to 12 GHz	25 mm to 37.5 mm
Ku band	12 to 18 GHz	16.7 mm to 25 mm
K band	18 to 27 GHz	11.1 mm to 16.7 mm
Ka band	27 GHz to 40 GHz	5.0 mm to 11.1 mm
Q band	33 to 50 GHz	6.0 mm to 9.0 mm
U band	40 to 60 GHz	5.0 mm to 7.5 mm
V band	50 to 75 GHz	4.0 mm to 6.0 mm
W band	75 to 110 GHz	2.7 mm to 4.0 mm
mm band	110 to 300 GHz	1 mm to 2.7 mm

Experimental and theoretical studies have been conducted to evaluate the effectiveness of various microwave frequency bands on soil moisture detection [11] [12] [13]. Low frequency (like the L band) is found to be more suitable for soil moisture detection because higher frequency microwave is very sensitive to vegetation and soil surface roughness [14] [15]. Microwave radiometry at 1.4GHz has been proved to be one of the most promising passive remote sensing techniques for retrieving soil moisture [16]. Different approaches have been developed to retrieve soil moisture from microwave data, such as empirical methods, semi-empirical methods, change detection methods, discrete scattering models, etc. [17]. The soil moisture, calculated through a microwave scattering model, mainly include Michigan Microwave Canopy Scattering model(MIMICS) used in vegetated areas and integral equation model (IEM), small perturbation model (SPM), physical optic model (POM), and geometrical optical model (GOM) in bare soil [18]. These models require a considerable amount of input parameters.

In general, passive microwave remote sensing is not suitable for accurate soil moisture detection in small regions due to its low spatial resolution; active microwave remote sensing is not suitable

for continuous soil moisture monitoring in a large scale due to its low temporal resolution [18]. In addition, the emissivity and backscattering coefficient of soil are sensitive to a lot of factors other than the soil moisture, such as the kind of land cover, surface roughness, soil texture, temperature, and so on [17] [19] [20]. This makes quantitative and accurate interpretation of the radiometric signal registered by the sensor very difficult.

Recently, combining the information obtained from multiple sources in the retrieval process, e.g., the synergistic use of active and passive microwave data, gained a lot of interest from researchers [17]. This is usually done by extracting information on roughness and vegetation properties from the active microwave data and then using this information to support the soil moisture retrieval from the passive microwave data [21] [22] [23] [24] [25] [26] [27].

Thermal Infrared Remote Sensing

The infrared region of the spectrum has a wavelength ranging from 700 nm to 1 mm in wavelength, which corresponds to frequency from 430 THz to 300 GHz. It is more common to refer to infrared in terms of wavelength rather than frequency. There are three main wavelength bands in infrared: shortwave infrared (SWIR) band (1.0-3.0 μm), mid-wave infrared (MWIR) band (3.0-5.0 μm), and long-wave infrared (LWIR) band (8-14 μm). The SWIR band utilizes reflected light and produces images identical to a black and white photo. The remote sensing using the SWIR, therefore, is generally categorized as optical remote sensing. The MWIR and LWIR bands actually provide thermographic images without an external light source and are often referred to as thermal infrared. The MWIR imaging has better contrast than LWIR imaging and provides more accurate details but less accurate temperature detection than LWIR imaging.

All objects with a temperature above absolute zero emit electromagnetic energy at all wavelength, as shown in Figure 4. The peak of the radiation spectrum for earth temperature objects falls in LWIR band, as shown in Figure 5.

Figure 4. Spectral intensity of blackbody radiation

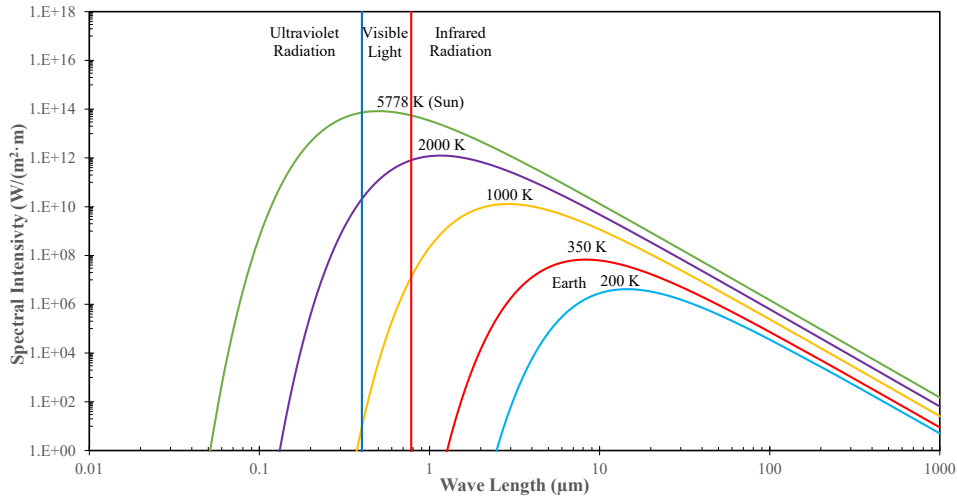
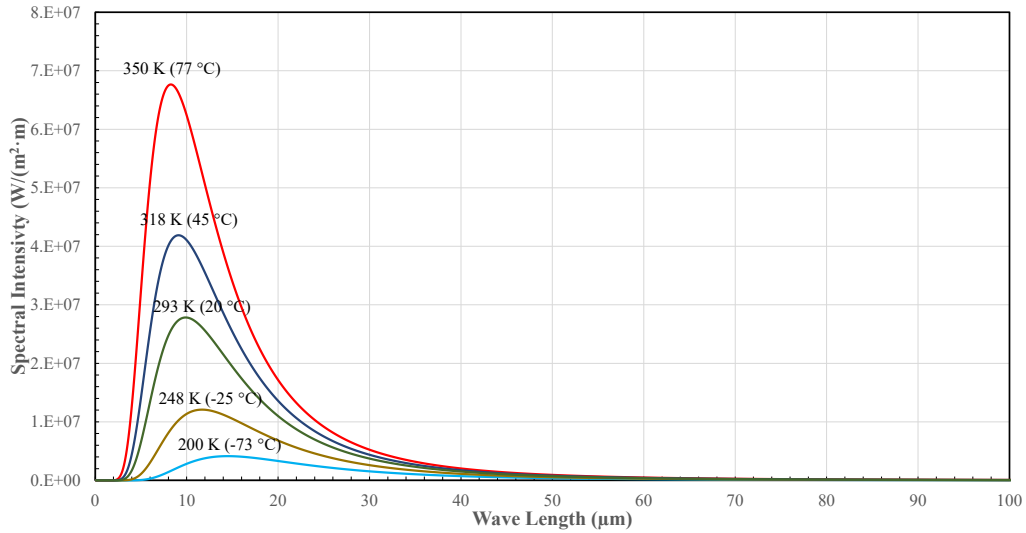


Figure 5. Spectral intensity of blackbody radiation at temperature of the Earth



Thermal infrared remote sensing has been used for surface soil moisture monitoring, mainly including the thermal inertia based method [28] and surface temperature based index method (e.g. crop water stress index (CWSI) [29]).

Thermal inertia (P) is defined as the square root of the product of soil thermal conductivity (λ_s), and volumetric heat capacity (C_s), i.e., $P = \sqrt{\lambda_s C_s}$. It measures the tendency of soil to resist change in temperature. Both soil thermal conductivity and volumetric heat capacity increase with the increase of soil moisture. Therefore, the higher the soil moisture content, the higher the

thermal inertia. In other words, soil with higher moisture content exhibits a lower diurnal temperature fluctuations.

The thermal inertia has been studied for soil moisture detection mostly by remote sensing researchers using the satellite data [30] [31] [32] [33] [34] [35]. In general, the thermal inertia-based methods for soil moisture estimation exploit the relationship between soil thermal inertial and the diurnal soil surface temperature variations [36]. The studies of thermal inertial based methods for estimating soil moisture in the literature can be grouped into four categories by relating the soil moisture to (1) the diurnal surface temperature amplitude directly [36], (2) the surface temperature gradient [37], (3) the thermal inertial retrieved from surface heat balance model with satellite thermal-infrared-based land surface temperature [38], (4) the apparent thermal inertial ($ATI = (1 - \alpha)/\Delta T$), where α is the surface albedo and ΔT is the diurnal surface temperature amplitude [39] [40]. Matsushima [28] conducted a comprehensive review of methods for estimating soil moisture using thermal inertia. He concluded that the thermal inertia based approach would be competitive with the assimilation method, which combines microwave soil moisture and satellite data from other spectral bands.

Since thermal inertial based methods are based on temperature changes, multiple soil surface temperature measurements over the diurnal course (i.e., temperature measurements in both daytime and nighttime) are required. The thermal inertia-based methods for soil moisture estimation have been based on passive radiometry measurements, of which the quantitative and accurate interpretation is very difficult. This method has spatial resolution of kilometers. The precision and accuracy of thermal inertia based methods are affected by the sky conditions, especially clouds and vegetation. Most of application of this method is not to rigorously determine the soil moisture content but instead to distinguish moisture deficient areas and thus aiding in irrigation and water management practice. Therefore, spatial soil moisture contrasts and temporal soil moisture changes (i.e., relative differences in soil moisture content), instead of actual soil moisture content, are more relevant in those research studies.

Surface temperature based index method can be based on the ratio of the actual evapotranspiration and potential evapotranspiration (e.g., CWSI) or the vegetation index/temperature trapezoid (VIT).

The crop water stress index (CWSI) was proposed by Jackson et al. [29] according to physiological functions of the plant and the principle of vegetation canopy energy balance and defined as:

$$CWSI = \frac{(T_c - T_a) - (T_c - T_a)_{min}}{(T_c - T_a)_{max} - (T_c - T_a)_{min}} \quad [1]$$

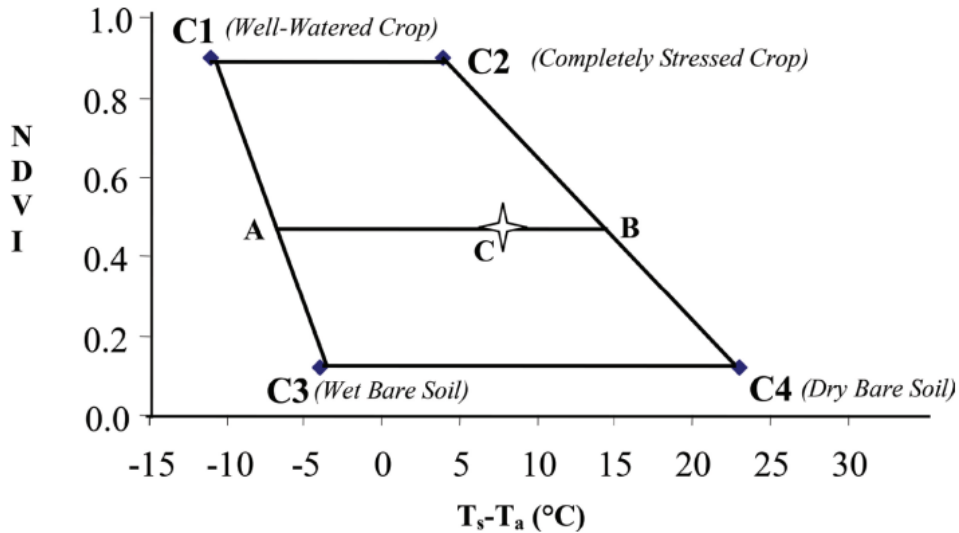
where, $(T_c - T_a)$ is the difference between measured canopy and air temperature, $(T_c - T_a)_{min}$ and $(T_c - T_a)_{max}$ are the theoretical upper and lower limits of $(T_c - T_a)$. It is, however, difficult to measure the canopy temperature of partially vegetated fields.

Due to the limitations of CWSI, Moran et al. [41] proposed water deficit index (WDI), which combines the vegetation index with surface-air temperature difference to form a VIT Trapezoid, as shown in Figure 6. The WDI is defined as the ratio of AC/AB in the figure as:

$$WDI = \frac{\overline{AC}}{\overline{AB}} = \frac{(T_s - T_a) - (T_s - T_a)_{min}}{(T_s - T_a)_{max} - (T_s - T_a)_{min}} \quad [2]$$

Both CWSI and WDI range from 0 to 1, with 0 indicating no water stress and 1 indicating maximum water stress.

Figure 6. VIT trapezoid [42]



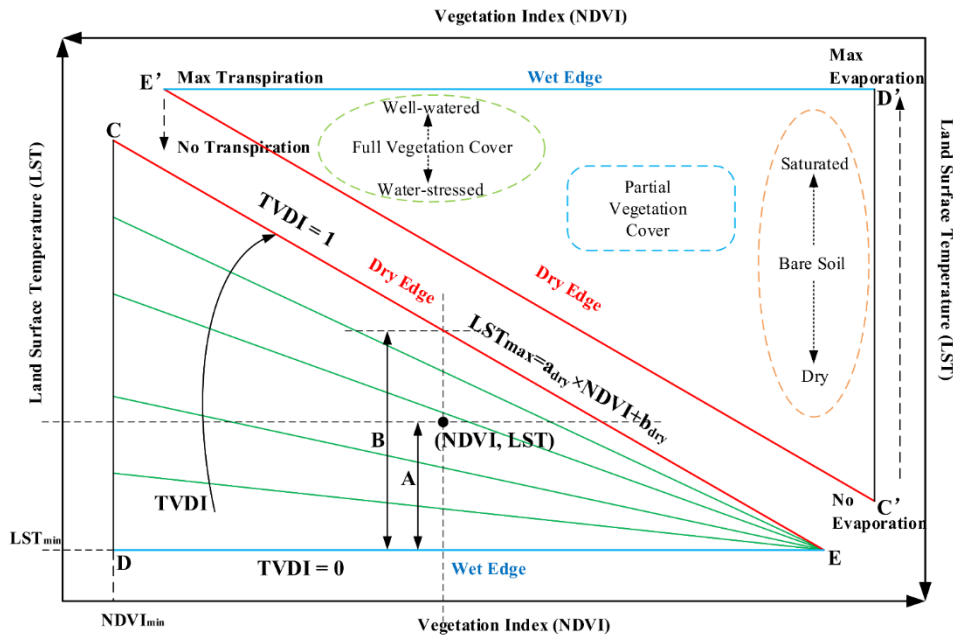
Temperature vegetation dryness index (TVDI) was proposed by Sandholt et al. [43] based on the concept that the land surface temperature responds slowly to changes in the soil moisture content when the vegetation coverage increases. TVDI combines the vegetation index with land surface temperature to form a Vegetation Index/Temperature (VIT) Triangle/Trapezoid, as shown in Figure 7. The TVDI is defined as:

$$TVDI = \frac{A}{B} = \frac{T_s - T_{smin}}{T_{smax} - T_{smin}}$$

[3]

As shown in Figure 7, TVDI ranges from 0 to 1. The higher the value of TVDI, the lower the soil moisture.

Figure 7. A Conceptual LST-NDVI triangle [44]



The temperature–vegetation index has been widely used as it considers the impact of surface soil, but the quantitative relationship between that and the true value of soil moisture is difficult to be determined; however, the method is suitable for large-scale areas.

The variation of emissivity with moisture content is mostly studied at microwave length, as the emissivity of soil is more sensitive to soil moisture in this spectral region [45]. Limited study has been done on variation of emissivity with soil moisture content in thermal infrared region [46] [47] [48] [49] [50] [51]. The first extensive study of variation of thermal infrared emissivity with moisture content was conducted by Mira et al. [45].

The study of the variation of infrared emissivity with soil moisture mainly aims at accurately estimating land surface temperature, which is an important parameter for net radiation budget and the surface energy balance. Though these studies have been important for understanding the influence of soil moisture content on emissivity, the effectiveness and applicability of using

emissivity to determine the moisture content quantitatively is an uncharted area, especially in engineering practice because the emissivity is affected by many other factors, such as roughness, soil types, etc. [52] [53].

Optical Remote Sensing

Optical remote sensing makes use of visible (380 nm to 750 nm), near infrared (NIR) (750 nm to 1.0 μm) and short-wave infrared (SWIR) (1.0 μm to 3.0 μm) sensors to detect the radiation reflected from the target surface. Figure 8 presents a typical spectral reflectance curve for a soil with different moisture contents, measured in the laboratory by Fabre et al. [54]. As shown in the figure, the reflectance values gradually decrease with the increase of the soil moisture and the decrease becomes less significant at high moisture levels. Patel [6] and Neema et al. [55], however, reported that the reflectance values first decreased with the increase of the soil moisture content and then increased after the soil moisture content exceeded a threshold value, which depended on soil types. Lobell and Asner [56] reported an exponential relationship between soil reflectance and degree of saturation. They also showed that reflectance approached horizontal asymptote at much lower moisture contents in the visible and NIR spectral regions than in the SWIR spectral region, i.e., longer wavelengths are better suited for soil with high moisture contents. Muller and Décamps [57] reported that the exponential relationship was valid for each soil but problematic when considering all soil together. This may be expected because soil reflectance is not just a function of moisture but is affected by many factors, such as soil type, amount of organic matter, particle size distribution, mineral composition, and color of soil elements [58]. Therefore, the single spectral analysis methods are difficult to apply for large-scale.

Figure 9 shows a typical spectral reflectance curve for a leaf with different moisture content measured [59]. As can be seen from the figure, water content also affects the reflectance of vegetation, mainly in NIR and SWIR bands. Gao et al. [18] proposed a method of estimating soil moisture in a vegetated area by constructing a two-dimensional space using red and NIR band reflectance. Direct surface soil reflectance was obtained by decomposition of mixture pixel reflectance. The empirical exponential relationship was then established between the surface soil reflectance and moisture content.

Figure 8. Measured spectra of a soil sample with different soil moisture [54]

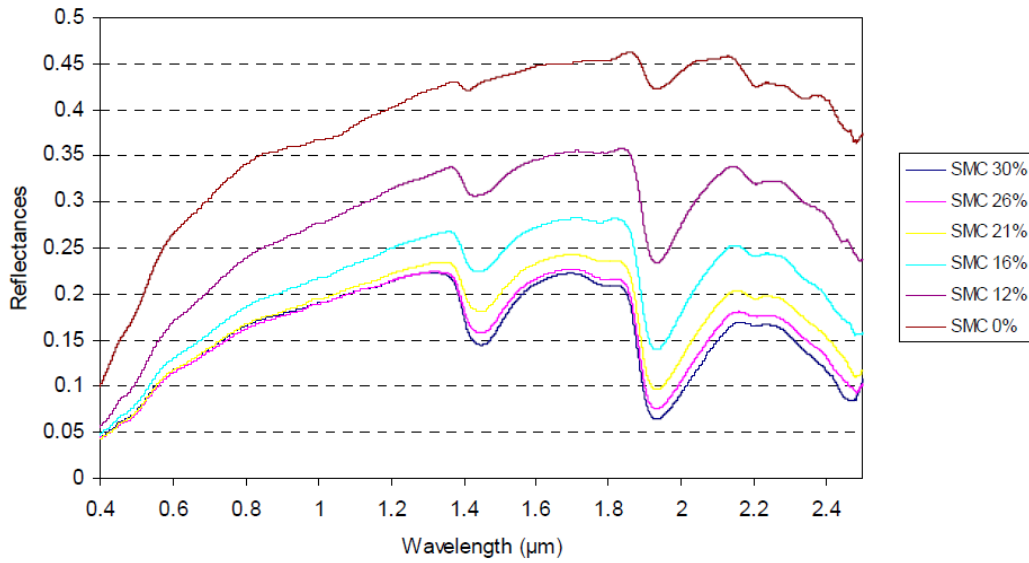
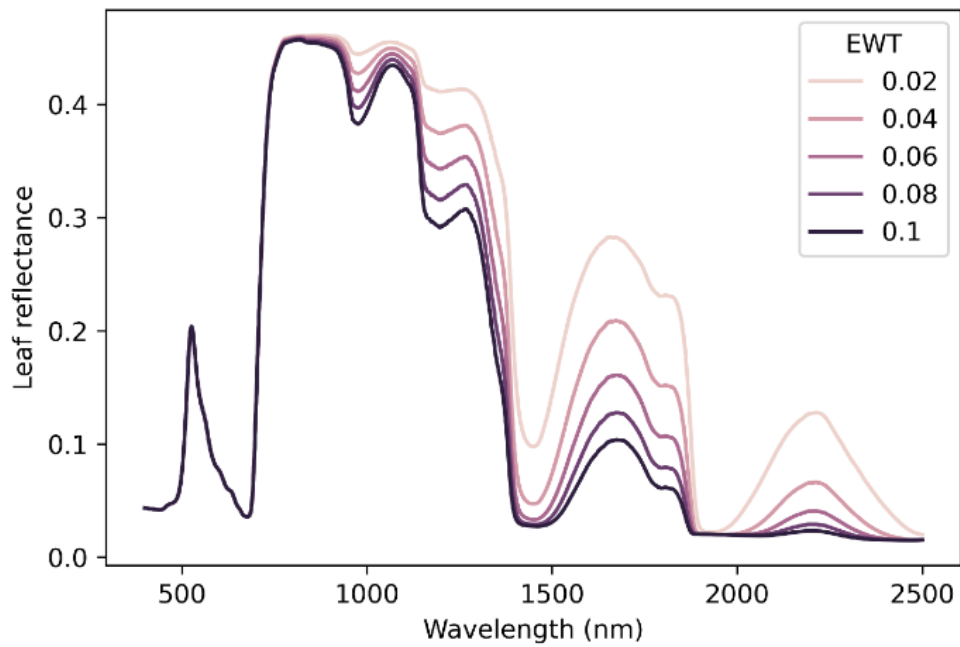


Figure 9. Simulated spectra of plant leaves with different equivalent water thickness (EWT) levels [59]



Various spectral indices that combine the reflectivity measurement with different spectral bands have been developed to for satellite-based high resolution remote-sensing soil moisture mapping.

These indices can be grouped into two categories: indices indirectly related to soil moisture and indices directly related to soil moisture.

Indirect soil moisture indices infer soil water content status through identifying vegetation cover condition [e.g., Normalized Difference Vegetation Index (NDVI), Green Normalized Difference Vegetation Index (GNDVI), Normalized Difference Water Index (NDWI), and Vegetation Condition Index (VCI)]. The water needed for vegetation growth is mainly absorbed from the soil. Vegetation condition is, therefore, a strong indicator of soil moisture condition, e.g., the insufficient soil moisture can cause vegetation failure. However, it should be pointed out that it is difficult to distinguish the effects of other environmental stress and adversities, e.g., diseases and pests [60].

Direct soil moisture indices have been proposed to estimate bare-soil moisture content directly [e.g., Water Index SOIL (WISOIL), Normalized Soil Moisture Index (NSMI), Normalized Index of N_{SWIR} domain for Soil Moisture estimation from Linear correlation (NINSOL), and Normalized Index of N_{SWIR} domain for Soil moisture content estimation from Nonlinear correlation (NINSON)] [54] [61] [62]. They are composed mainly of NIR and SWIR bands, which provide a higher saturated soil moisture than the visible bands. These indices have been validated by reflectance measurements in the laboratory by different researchers [54] [63]. The main drawback of these indices is the use of bands located in the water vapor absorption bands [54].

NDVI is computed as the difference between near-infrared (NIR) and red (RED) light reflected by the object as:

$$NDVI = \frac{NIR-RED}{NIR+RED} \quad [4]$$

GNDVI is computed as the difference between near-infrared (NIR) and green (GREEN) light reflected by the object as:

$$NDVI = \frac{NIR-GREEN}{NIR+GREEN} \quad [5]$$

The short-wave infrared (SWIR) band is sensitive to the water content of the plants; it is an important band for drought monitoring by remote sensing. The normalized difference water index (NDWI) proposed by Gao [64] is computed using the near infrared and SWIR reflectance as:

$$NDWI = \frac{NIR-SWIR}{NIR+SWIR} \quad [6]$$

NDWI varies between -1 to +1, depending on the leaf water content but also on the vegetation type and cover. High values of NDWI indicate sufficient moisture content, while low NDWI values indicate water stress. NDWI has been widely used for drought monitoring. However, the method is not suitable for bare soil areas and sparsely vegetated areas [65].

The other variant of NDWI proposed by [66], which uses green and NIR bands, has been mainly used for water body mapping [67]. It is based on the fact that the reflectance of clear water is the highest in the green band, decreases with increasing wavelength, and reaches a value close to zero in the NIR band.

The vegetation condition index (VCI) proposed by Kogan [68] is expressed as NDVI anomaly relative to a specific climatology and computed as:

$$VCI = \frac{NDVI - NDVI_{min}}{NDVI_{max} - NDVI_{min}} \quad [7]$$

$NDVI_{max}$ and $NDVI_{min}$ are multiple year maximum and minimum NDVI for pixel with reference to a specific climatology.

WISOIL is computed using the SWIR reflectance at 1.45 μm and 1.3 μm as:

$$WISOIL = \frac{SWIR_{1.45 \mu\text{m}}}{SWIR_{1.3 \mu\text{m}}} \quad [8]$$

NSMI is computed using the SWIR reflectance at 1.8 μm and 2.119 μm as:

$$NSMI = \frac{SWIR_{1.8 \mu\text{m}} - SWIR_{2.119 \mu\text{m}}}{SWIR_{1.8 \mu\text{m}} + SWIR_{2.119 \mu\text{m}}} \quad [9]$$

NINSOL is computed using the SWIR reflectance at 2.076 μm and 2.23 μm as:

$$NINSOL = \frac{SWIR_{2.076 \mu\text{m}} - SWIR_{2.23 \mu\text{m}}}{SWIR_{2.076 \mu\text{m}} + SWIR_{2.23 \mu\text{m}}} \quad [10]$$

NINSON is computed using the SWIR reflectance at 2.122 μm and 2.23 μm as:

$$NINSON = \frac{SWIR_{2.122 \mu\text{m}} - SWIR_{2.23 \mu\text{m}}}{SWIR_{2.122 \mu\text{m}} + SWIR_{2.23 \mu\text{m}}} \quad [11]$$

Synergistic use of multi-type remote-sensing data to estimate soil moisture content has also gained a lot of interest from researchers, e.g., microwave and thermal infrared [69], microwave and optical [70], thermal infrared and optical [71], and microwave, thermal and optical [72].

In summary, studies on estimating soil moisture content using remote sensing technology are still in the qualitative stage, i.e., classify areas into a few levels of soil moisture (e.g., wet, middle,

dry) due to complex influence factors. The satellite sensor is generally used in those studies and has a resolution of kilometers. These issues challenge the applicability of remote sensing technology to engineering practice, which often requires very high spatial resolutions (cm to m) and quantification of moisture content. The advancement of remote sensing technology has now allowed sensors to be used in the laboratory or installed on drone platform, opening up the opportunity to apply this technology in engineering practice.

Objective

The objective of this research study was to evaluate the capability of drone-mounted remote sensors to estimate soil moisture and its spatiotemporal variability in embankment/dam, thus, assess the feasibility of using remote sensing technologies to evaluate the risk of slope failure of the embankments/dam.

Scope

Two drone cameras were evaluated in this study: FLIR Vue Pro R, a radiometric thermal camera, and MicaSense RedEdge, a multispectral camera for precision agriculture. Specifically, they were evaluated both in laboratory and field settings for their accuracy, repeatability, and reliability.

Laboratory testing was carried on an embankment soil to evaluate the sensitivity of the thermal camera on soil moisture under various conditions. The effect of camera mounting height and camera heating on thermal readings was also evaluated in the laboratory. Field testing was first conducted at the Pavement Research Facility (PRF) of the Louisiana Transportation Research Center (LTRC) to further test the capabilities and limitations of both thermal and multispectral cameras. The testing was focused on a soil embankment approximately 150 ft. long and 20 ft. high. The soil embankment slope was divided into different moisture zones by wetting them with a predetermined amount of water for each zone. The image data of the slope was captured by both the thermal and multispectral camera. A stand-alone geotagging module was also tested to automatically geotag the thermal images during the field testing at PRF.

Finally, the field data were collected at I-10 @ LA30 embankment site using both thermal camera and multispectral camera and at Iatt Lake Dam and Vernon Lake Dam using only the thermal camera.

Methodology


This research explores the capabilities of drone-mounted remote sensing sensors for soil moisture detection on embankment soils for their accuracy, repeatability, and reliability. Two drone cameras are evaluated in this study: FLIR Vue Pro R, a radiometric thermal camera, and MicaSense RedEdge, a multispectral camera for precision agriculture. Specifically, they were evaluated both in laboratory settings on an embankment soil and field settings at various embankment/dam sites.

Drone-Mounted Remote Sensing Sensors

Thermal Camera

The FLIR Vue Pro R is a thermal camera for small Unmanned Aircraft Systems (sUAS). It can capture accurate, non-contact temperature measurements from an aerial perspective and save images with calibrated temperature data embedded in every pixel. Its output is temperature reading as well as thermal images of a subject. This camera is capable of taking one image per second with specifications as indicated in Table 2.

Table 2. FLIR Vue Pro R thermal camera specifications

	
Size: 2.26 in. x 1.75 in. (including lens)	Operational Altitude: +40,000 ft.
Full Frame Rate: 30 Hz (NTSC); 25 Hz (PAL)	Operating Temperature Range: 20°C to +50°C (-4°F to 122°F)
Sensor Resolution: 336 × 256	Measurement Accuracy: +/-5°C or 5% of reading (+/- 9°C)
Color palettes: Yes – Adjustable	Spectral Band: 7.5 - 13.5 μm
Stores as JPEG/MJPEG on Micro SD Card	

The FLIR Vue Pro R camera is used in this study due to the reality that there is no remote sensor available on the market that can directly measure soil moisture content, and also with the understanding for a thermal camera as follows. All objects emit infrared radiation as a function of their temperature. A thermal camera measures infrared radiation and converts it into an electronic image that shows the apparent surface temperature of the object being measured. Figure 10 depicts the process of measuring soil's infrared radiation. The total radiation received by a thermal camera (I_t) includes the radiation directly emitted from the target object (soil) (I_{obj}), the radiation emitted from the any ambient sources that reflected off the target object (I_{refl}), and the radiation emitted from the atmosphere (I_{atm}) (14), i.e.,

$$\begin{aligned} I_t &= I_{obj} + I_{refl} + I_{atm} \\ &= \tau \times \varepsilon \times \sigma \times T_{obj}^4 + \tau \times (1 - \varepsilon) \times \sigma \times T_{refl}^4 + (1 - \tau) \times \sigma \times T_{atm}^4 \end{aligned} \quad [12]$$

where, τ is the transmittance of the atmosphere, ε is the emissivity of the target object, σ is the Stefan–Boltzmann constant ($\sigma = 5.67 \times 10^{-8} \text{ W/m}^2/\text{K}^4$), $(1 - \varepsilon)$ is the reflectance of the target object, $(1 - \tau)$ is the emissivity of the atmosphere, T_{obj} is the temperature of the target object in Kelvin (K), T_{refl} is the equivalent temperature of the ambient sources in Kelvin (K), and T_{atm} is the temperature of the atmosphere in Kelvin (K). Assuming all ambient sources to be at the same temperature of T_{refl} is of course a simplification of the true situation. T_{refl} , however, can, at least theoretically, represent an equivalent temperature of a complex surrounding. It is also a necessary simplification in order to apply infrared thermography in practice. The transmittance of the atmosphere is calculated as follows in the FLIR system (15):

$$\tau = X \cdot e^{[-\sqrt{d} \cdot (\alpha_1 + \beta_1 \cdot \sqrt{w})]} + (1 - X) \cdot e^{[-\sqrt{d} \cdot (\alpha_2 + \beta_2 \cdot \sqrt{w})]} \quad [13]$$

$$w = RH \cdot e^{(1.5587 + 6.939 \cdot 10^{-2} \cdot T_{atmC} - 2.7816 \cdot 10^{-4} \cdot T_{atmC}^2 + 6.8455 \cdot 10^{-7} \cdot T_{atmC}^3)} \quad [14]$$

where, X is the scaling factor for the atmosphere damping (=1.9), d is the distance to the target object, w is the coefficient indicating the content of water vapor in the atmosphere, α_1 , α_2 is the attenuation for atmosphere without water vapor, β_1 , β_2 is the attenuation for water vapor, RH is the relative humidity, T_{atmC} is the temperature of atmosphere in Celsius ($^{\circ}\text{C}$).

For laboratory settings, i.e., short distance, the third components can be neglected and Equation (1) can be reduced as Equation (2):

$$I_t = \varepsilon \times \sigma \times T_{obj}^4 + (1 - \varepsilon) \times \sigma \times T_{refl}^4 \quad [15]$$

The reasons that the thermal camera was chosen for this study was based on the thermal characteristics of earth materials and infrared thermography for the following considerations:

- The emissivity of soil is a function of moisture content.

- Thermal inertia varies with soil moisture content. An increase in soil moisture generally increases the thermal inertia of that soil as air in the pore spaces of the soil are replaced by water. As such, soils with different moisture content heats up and cools down at different rates during the day and night, thus giving rise to different diurnal cycle of temperature fluctuations as shown in Figure 11.
- In the seepage area, the water from a reservoir flows through soils and reappears downstream of the dam. This subsurface seepage water is supposed to be cooler than the soil surface during hot weather and warmer than the soil surface during the cold weather.

It is ideal if a thermal camera can capture the variation of soil moisture content and demonstrate it in the images. This was studied both qualitatively and quantitatively first in the laboratory and then in the field using the FLIR Vue Pro R camera.

Figure 10. Principle of a thermal camera detecting infrared radiation from soil

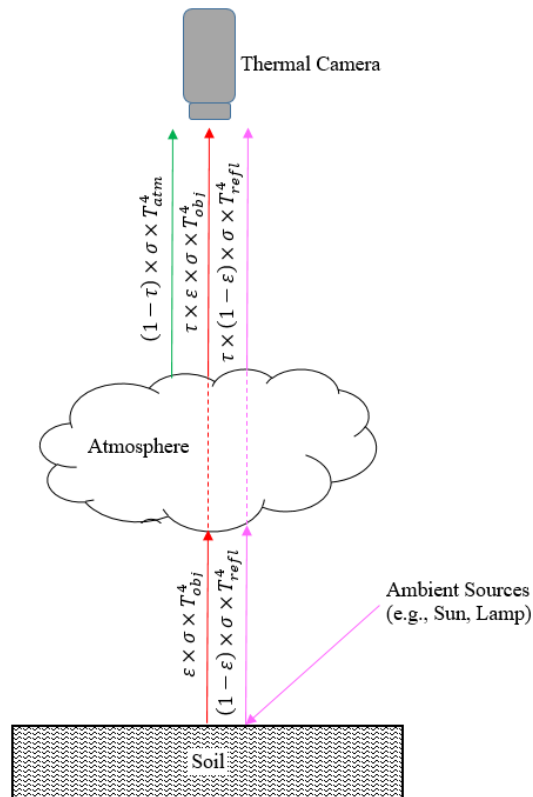
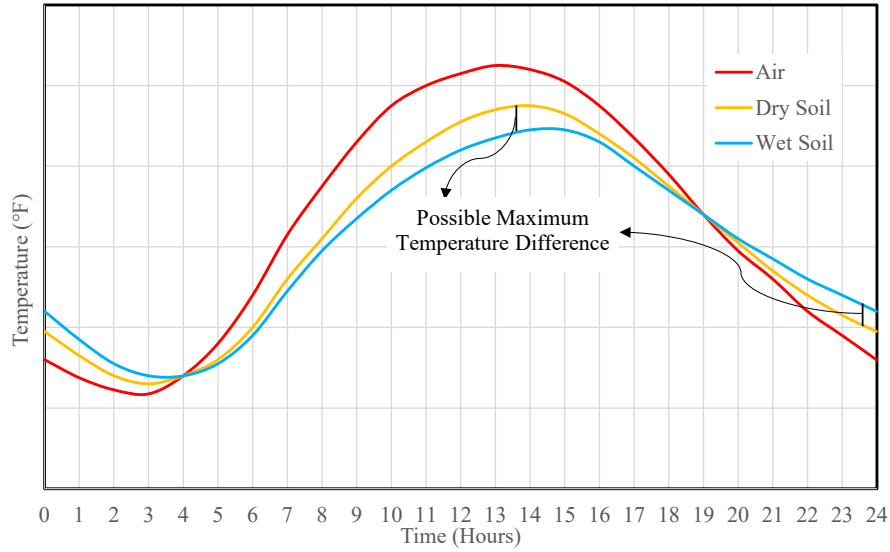


Figure 11. Effect of thermal inertia on diurnal soil surface temperature variation



RedEdge™ Multispectral Camera

The RedEdge™ multispectral camera has a lightweight of 150 g and small dimensions of 12.1 cm × 6.6 cm × 4.6 cm. At the maximum flight height of 120 m, the sensor offers an 8 cm ground sampling distance (spatial resolution). The capture rate of this camera is 1 capture per second with an option of 12-bit raw imaging format. Table 3 presents the camera's specifications.

A multispectral camera detects radiation reflected by the object within specific wavelength regions across the electromagnetic spectrum; therefore, it requires an external light source such as sunlight to illuminate the object surface, as indicated in Figure 12. In our case, it consists of recording the images of the object in the blue, green, red, red edge, and near infrared bands, as shown in Table 4. The appeal of multispectral remote sensing is that objects that are indistinguishable at one wavelength may be easy to tell apart at other wavelengths.

The pixel value (i.e., intensity value in a pixel) is known as the raw unprocessed image. The Digital Number (DN) is commonly used to describe pixel values. The RedEdge camera can save images in 12-bit or 16-bit format. For 12-bit images, the DN ranges from 0 to 4096. For 16-bit images, the DN ranges from 0 to 65536. The image in its original DN values is not physically meaningful.

The RedEdge provides a tool called radiometric calibration which converts the DN values into absolute spectral radiance values. The formula for conversion is:

$$L = V(x, y) \frac{a_1}{g} \frac{p - p_{BL}}{t_e + a_2 y - a_3 t_e y} \quad [16]$$

Where, p is the normalized raw pixel value (for 16-bit images, divide by 65536; for 12-bit images, divided by 4096); p_{BL} is the normalized black level value (can be found in metadata tags); a_1, a_2, a_3 are the radiometric calibration coefficients; $V(x, y)$ is the vignette polynomial function for pixel location (x, y) ; t_e is the image exposure time; g is the sensor gain setting (can be found in metadata tags); x, y are the pixel column and row number, respectively; L is the spectral radiance in $W/m^2/sr/nm$.

The RedEdge provides a Calibrated Reflectance Panel (CRP) to convert radiance to reflectance, which is the fraction of incident radiation that is reflected from a surface. The transfer function of radiance to reflectance to the i^{th} band is:

$$F_i = \frac{\rho_i}{avg(L_i)} \quad [17]$$

Where F_i is the reflectance calibration factor for band i ; ρ_i is the average reflectance of the CRP for the i^{th} band; $avg(L_i)$ is the average value of the radiance for the pixels inside the panel for band i . This factor can be used for the i^{th} band to convert all radiance values to reflectance by simply multiplying the radiance values by the factor F_i .

Reflectance maps can then be converted to index maps such as NDVI for different applications.

Table 3. RedEdge TM multispectral camera specifications

Resolution	1280 × 960
Lens	5.5 mm
Horizontal Field of View (HFOV)	47.2°
Vertical Field of View (VFOV)	36.2°

Figure 12. Principle of a multispectral camera detecting radiation reflected by soil

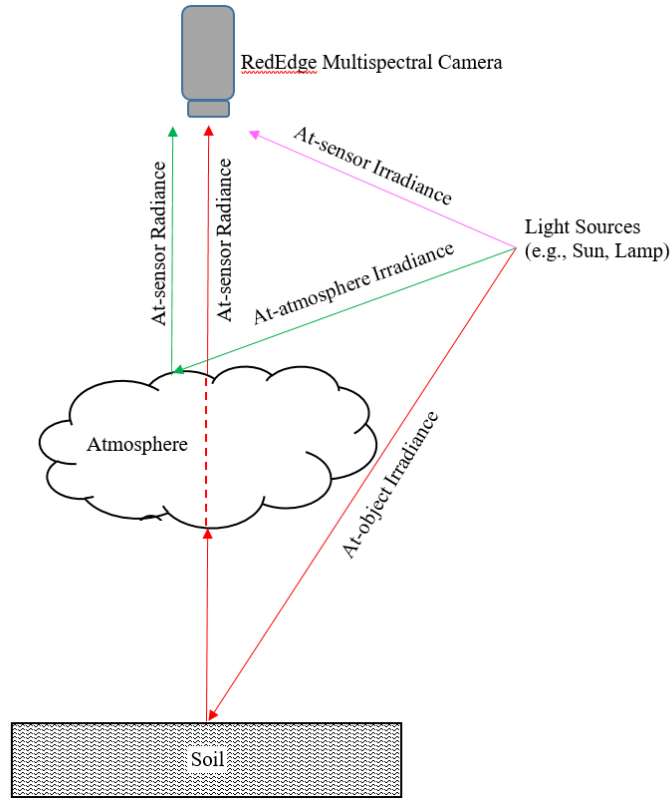


Table 4. Spectral bands of RedEdge TM multispectral camera

Band Number	Band Name	Center Wavelength (nm)	Bandwidth FWHM (nm)
1	Blue	475	20
2	Green	560	20
3	Red	668	10
4	Near IR	840	40
5	Red Edge	717	10

Laboratory Testing

Laboratory testing is divided into two phases. During phase I, a series of preliminary tests were first conducted to evaluate the effect of camera mounting height and camera heating effect on thermal readings and develop a testing procedure. During phase II, based on what we learned from phase I,

The embankment soil used in this study had a liquid limit of 33 and a plastic index of 12. The maximum dry density of the soil, as determined by Standard Proctor test, was $1,698 \text{ kg/m}^3$ with an optimum moisture content of 17.3%. This embankment soil was classified as CL and A-5 according to the Unified Soil Classification System (USCS) and the AASHTO classification system, respectively. The amount of water for each soil sample tested in the lab was first calculated based on the target moisture contents from 0% to 40% at 5 percent increment. The soil samples were prepared by hand mixing the soil with water pre-determined to target various moisture contents. Then, the soil was spread in the pan with the size of 8 in.x10 in. Once all soil samples with nine different moisture contents were prepared, they were arranged in 3 rows and 3 columns and placed on a working bench. Images were then acquired. After that, the soil was removed from the pan and placed in plastic bags for overnight. Next day, the soil was removed from the plastic bags and spread in the pan again. Images were acquired again. Figure 13 shows the testing setup and soil samples used in the laboratory testing.

Figure 13. Laboratory testing setup



a



b

Field Testing at Pavement Research Facility Site

The field testing was conducted at the Pavement Research Facility (PRF) of Louisiana Transportation Research Center (LTRC), (Figure 14a), which is located on a six-acre site near LA 1 south, across the Mississippi River from Baton Rouge. During the field testing, the FLIR Vue Pro R, as shown in Figure 14b, was mounted on a DJI inspire 2 drone, which was

programmed to fly along the certain path at different altitudes. The testing was focused on a soil embankment about 150 ft. long and 20 ft. high, as shown in Figure 14-c and -d. A grid flight path is designed to be sure that each following image overlaps the previous by 75%, both in the forward direction (i.e., frontlap) as well as the side direction on the parallel track (i.e., sidelap). Figure 15 shows a typical flight path used to cover the soil embankment and its surrounding area in this study. A total of five flight sessions has been conducted. Flight sessions 1 and 2 were trial-and-error sessions. In flight session 3, the soil embankment slope were divided into three moisture zones. In flight sessions 4 and 5, the soil embankment slope was divided into five moisture zones and a geotagger attached to the FLIR Vue Pro R thermal camera was tested.

Figure 14. Drone flight testing site at PRF



a



b



c



d

Figure 15. A typical flight path at PRF site



Field Testing at I-10 @ LA30 Embankment Site

The site includes four embankments, the eastbound west approach embankment, the eastbound east approach embankment, the westbound west approach embankment, and the westbound east approach embankment, constructed for the I-10 Interchange bridge at LA30. The site is located near Gonzales in Ascension Parish. There is a 100-ft long surface sliding failure area on the eastbound west approach embankment between eastbound and westbound I-10, which makes it a good site for this study. Figure 16 presents an aerial view of the embankment site. A close view of the sliding failure area is shown in Figure 17. Due to the site conditions, limitations of the drone, and drone regulations, the entire site is divided into 6 regions and covered with 6 flights for each remote sensing sensor, as shown in Figure 18. The flight path for each flight is also included in Figure 18.

Figure 16. Aerial view of I-10 @ LA30 embankment site



Figure 17. A close view of sliding failure area



Figure 18. Flight paths for I-10 @ LA30 embankment site



Field Testing at Iatt Lake Dam Site

Iatt Lake Dam is located in Grant Parish. The dam consists of 1,750-ft. long aggregate roadway on native soil earthen embankment that runs along the southwestern shoreline of Iatt Lake. The crown width is 12 ft. The upstream slope descends from the crown at a 3H:1V rate, and the downstream slope descends from the crown at a 4H:1V rate. Figure 19 presents an aerial view of Iatt Lake Dam site. The flight paths are shown in Figure 20.

Figure 19. Aerial view of Iatt Lake Dam

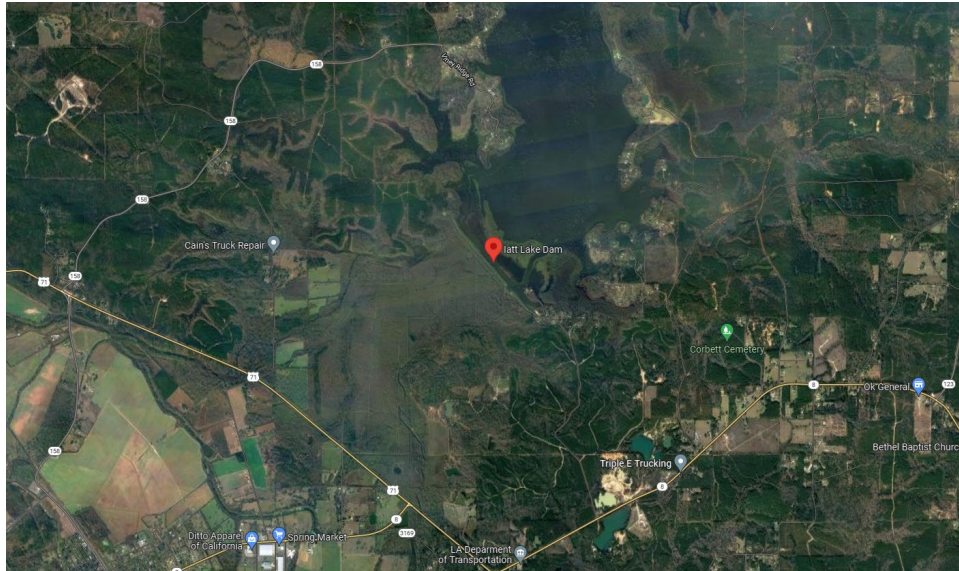
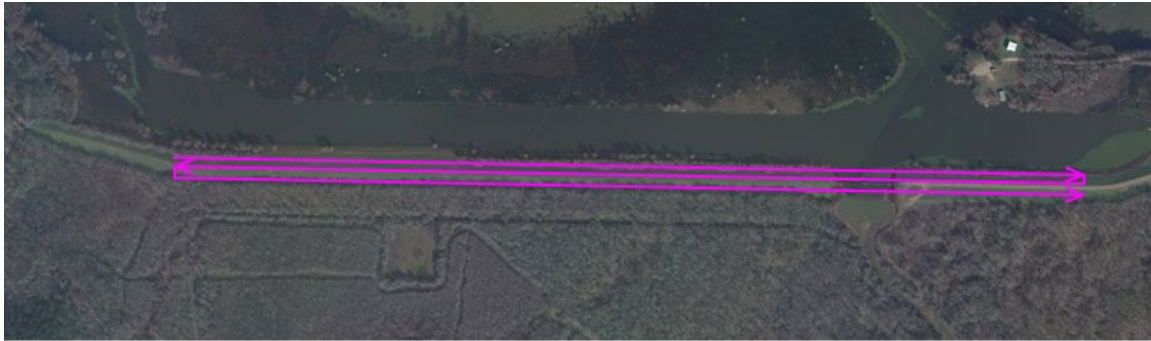


Figure 20. Flight path for Iatt Lake Dam



Field Testing at Vernon Lake Dam Site

Vernon Lake dam is located in Sections 1 and 2 of Township 2 North, Range 10 West in Vernon Parish, about 6 miles northwest of Leesville, Louisiana. The dam can be found on USGS Quadrangle Maps 106A and 106B. The Vernon Lake Dam consists of a 5,275-ft. long earthen embankment that runs along the southern portion of the reservoir. The crown width is 16 ft. The upstream slope descends from the crown at a 3H:1V rate, and the downstream slope descends from the crown at a 4H:1V rate. Figure 21 presents an aerial view of Vernon Lake Dam site. The flight paths are shown in Figure 22.

Figure 21. Aerial view of Vernon Lake Dam

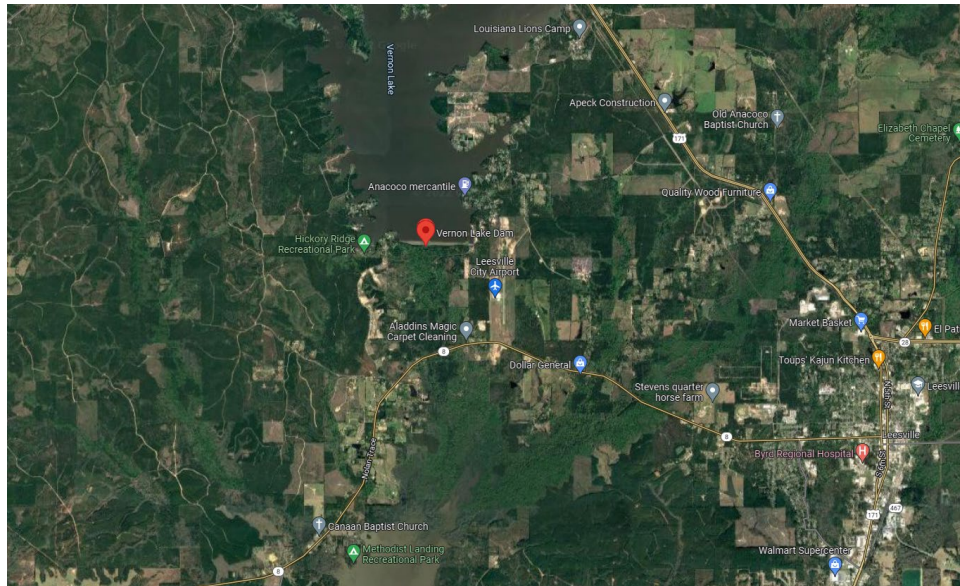
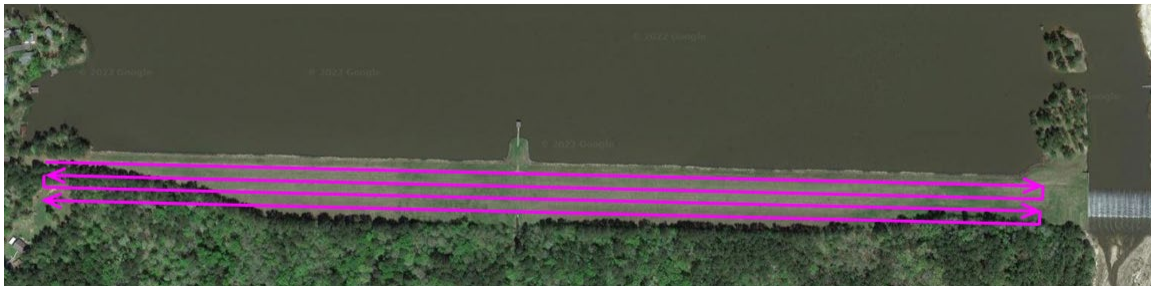


Figure 22. Flight paths for Vernon Lake Dam



Discussion of Results

Laboratory Testing

Preliminary Tests

The effect of thermal camera mounting height was investigated using a metal pan with 0.5 in. of water and a polypropylene bucket filled with 8 in. of water. Table 5 presents the thermal readings at different heights. It can be seen that the thermal readings are almost constant for water in both containers regardless of height, with coefficient of variation less than 1.5%. However, there is a consistent difference between the thermal readings for water in the pan and in the bucket, although both are at equal temperatures. This may be due to different water depths.

Table 5. Temperature readings at different heights

Height (ft.)	Thermal Reading (°F)		Difference (°F)
	Pan	Bucket	
3	82.3	85.5	3.2
6	83.4	85.2	1.8
9	82.4	85.4	3.0
12	81.5	85.2	3.7
Average	82.4	85.3	
COV (%)	1.2	0.2	

The researchers conducted an experiment (no light) for the thermal camera warm up time, i.e., the time needed to achieve best temperature measurement accuracy after powering on the camera. An image of a target was taken every one minute from the time when the camera was turned on and ready for imaging. The derived result in Figure 23 showed that the camera reached relatively stable temperature readings after around 30 min. Therefore, the research team determined to acquire thermal imaging after the thermal camera had been turned on for at least thirty minutes. In the field, when multiple flights are conducted, the camera often has to be turned off for a battery change. The researchers conducted another experiment (no light) for the battery change effect and took an image of a target every one minute, including before and after the battery change. Figure 24 indicated that after the battery change, there is a sudden drop in temperature readings and it took about five minutes for the camera to return to its original

temperature readings. Figure 23 and Figure 24 also show that the camera can provide a precision of $\pm 1^{\circ}\text{F}$ under lab conditions.

Figure 23. Examination of camera warmup time

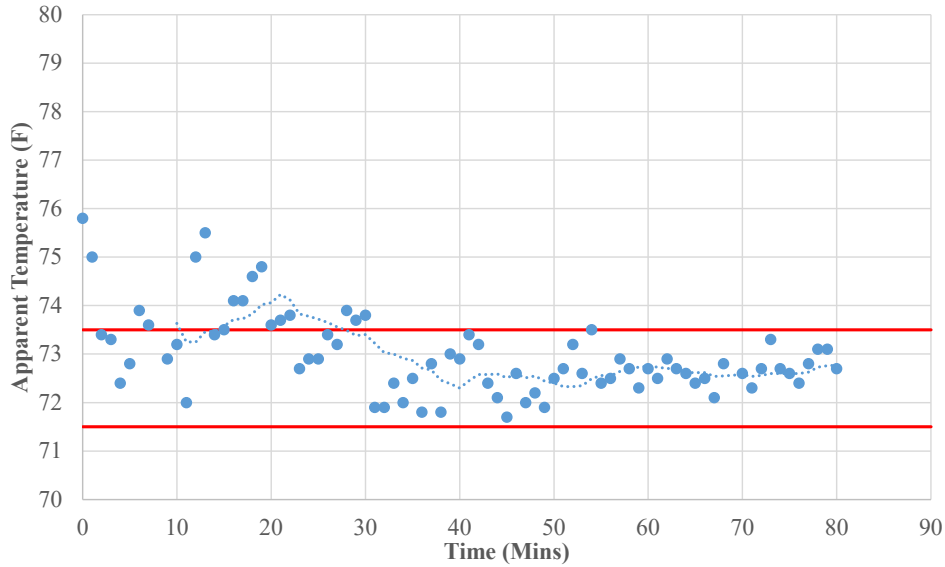
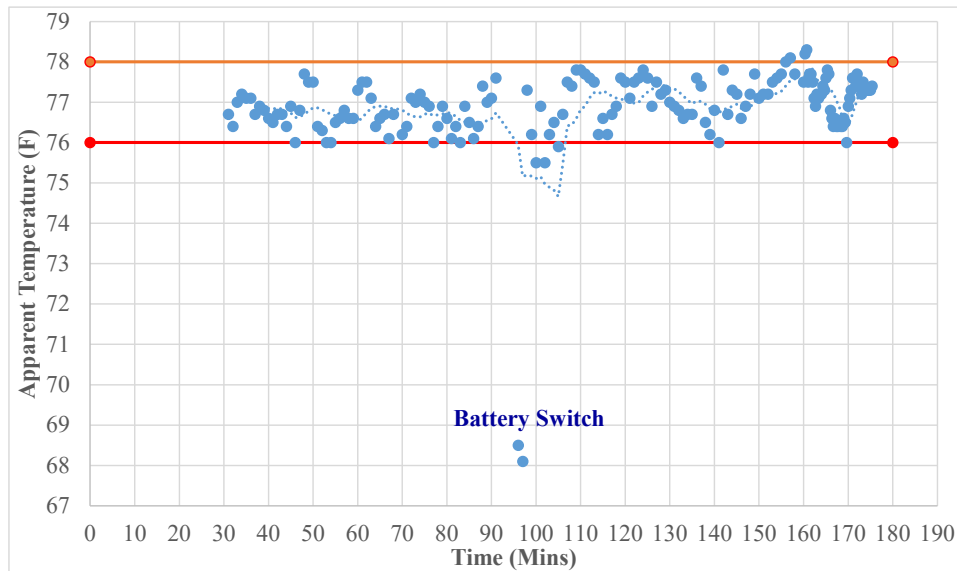


Figure 24. Examination of camera battery change effect



A series of tests were conducted to try different test setups. Initially, we prepared a soil sample in dry condition in a pan. The moisture content of the soil sample was increased in 5% increments until it reached 40%. Thermal images were taken at each increment. Inconsistent data were

obtained due to various reasons, such as non-uniform moisture distribution, varied ambient sources, etc. After a series of trial and error, we finally developed a test setup (Figure 13) and a test procedure that were used in all lab tests. In this test setup, nine pans of soil sample with different moisture contents were arranged in a 3×3 array so all soil sample could fit in a single thermal image. The soil sample was prepared by mixing soil with pre-determined water in a pan to achieve the target moisture content. The soil was then spread out in the pan for a thermal image. After the thermal image was taken, the soil was placed in a plastic bag. In the next day, the soil was taken out of the bag and spread out in the pan for another thermal image. The temperature of water used to make soil samples affected the thermal readings of soil samples immediately after mixing and thus thermal readings of day 1 soil samples are not included here.

Main Tests

Equation (2) can be rearranged to give an expression for T_{obj} .

$$T_{obj} = \sqrt[4]{\frac{I_t - (1-\varepsilon) \times \sigma \times T_{refl}^4}{\varepsilon \times \sigma}} \quad [18]$$

This means that the measured temperature will only be accurate if the emissivity value and the equivalent background temperature are set to the correct value. However, the emissivity value of soil sample in this study is unknown. Figure 25 shows the measured apparent temperatures of soil samples at different moisture contents obtained from a series of tests, with an emissivity setting of 1. In this case, the total radiation received by a thermal camera (I_t) is calculated as:

$$I_t = \sigma \times T_{measured}^4 \quad [19]$$

Combine Equations (2) and (3), then:

$$\sigma \times T_{measured}^4 = \varepsilon \times \sigma \times T_{obj}^4 + (1 - \varepsilon) \times \sigma \times T_{refl}^4 \quad [20]$$

The equation can be rearranged to give an expression for $T_{measured}$.

$$T_{measured} = \sqrt[4]{\varepsilon T_{obj}^4 + (1-\varepsilon) T_{refl}^4} \quad [21]$$

As seen from Equation (5), when the radiation emitted by soil samples is the same as radiation emitted by its surroundings (i.e., $T_{obj} = T_{refl}$), the measured temperature is always the same as the temperature of the surface of soil sample, independent of emissivity value. However, in most situations, the radiation emitted by soil samples differs from the radiation emitted by its

surroundings, such as a warm soil sample in a cold environment or a cold soil sample in a warm environment. In this case, when we interpret the measured temperature, we need to pay extra attention to reflected temperature. As emissivity decreases, what we are measuring is coming more from the surfaces of surrounding objects (including the camera and operator), not the soil sample we are inspecting. Figure 26 demonstrates how the reflected temperature affects the measured temperature. With a soil surface temperature higher than the background temperature, the measured temperature increases with an increase of emissivity values. Thus with a soil surface temperature lower than the background temperature, the measured temperature decreases as the emissivity values increase. As shown in the literature review, the emissivity of soil increases with the increase of moisture content. For silty clay the range of emissivity can vary from 0.9 to 0.98. By observing the Figure 26, it is apparent that the reflected temperature is higher than the soil surface temperature in this study. The decreasing trend of measured temperature is obvious when the moisture content is less than 15%. This may be because that the emissivity values of soil samples in this study only noticeably increases with moisture content up to 15%. After that, the relationship curve gets flatter. It also should be pointed out here that the soil surface roughness is more consistent for soil on the dry side than on the wet side as shown Figure 27. This may explain why no consistent results were observed when the moisture content is beyond 15%. Further study is needed to understand how soil surface roughness affects the emissivity value of a soil sample.

Figure 25. Apparent temperature vs moisture content

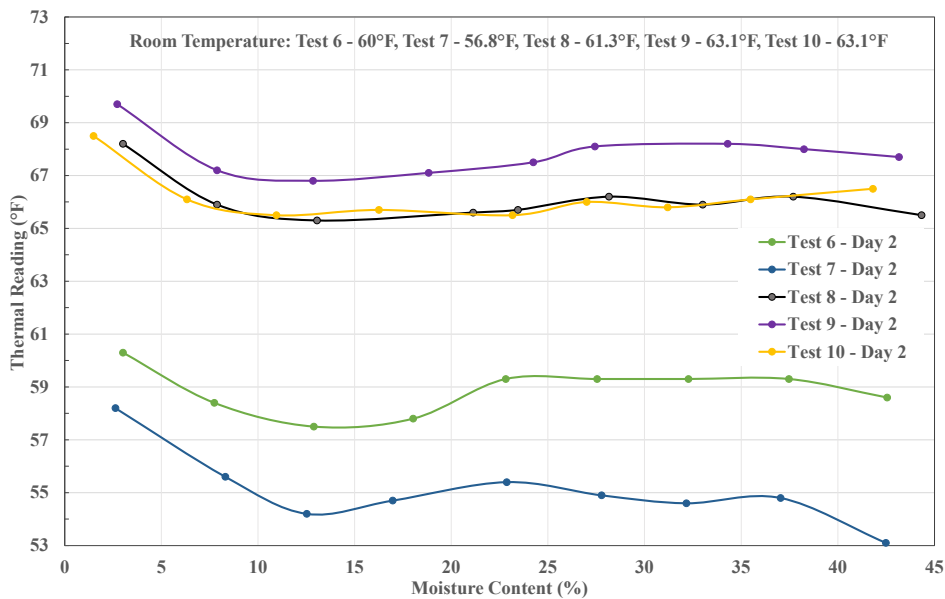
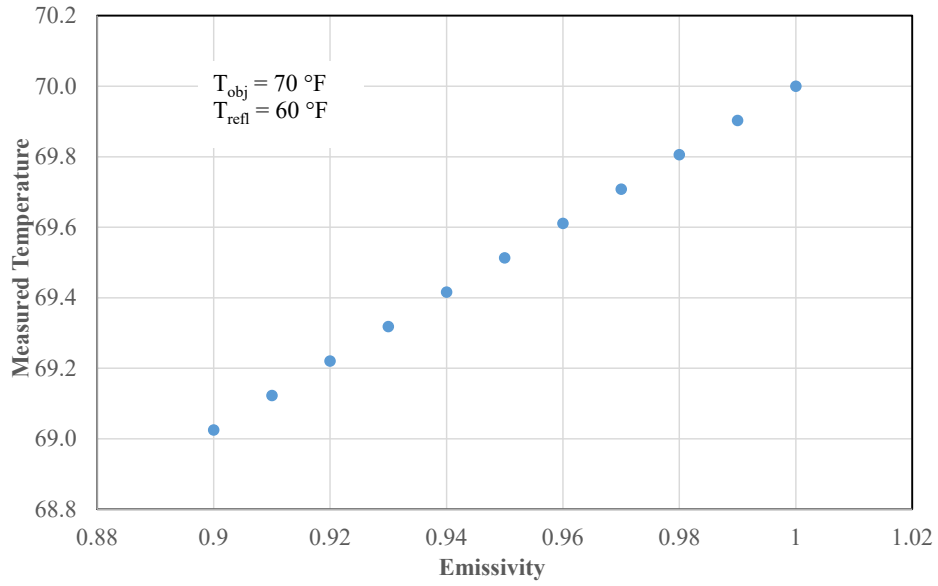
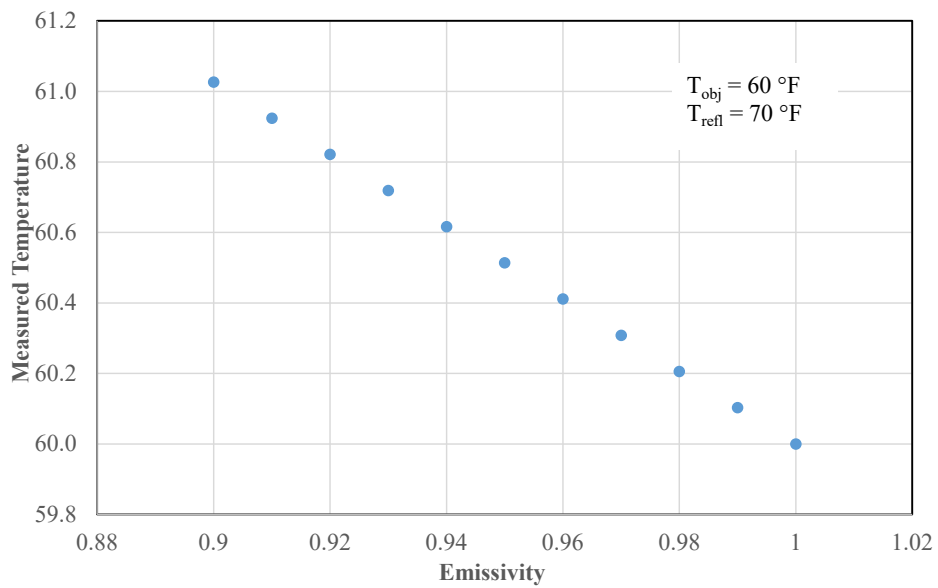


Figure 26. Measured temperature vs. emissivity

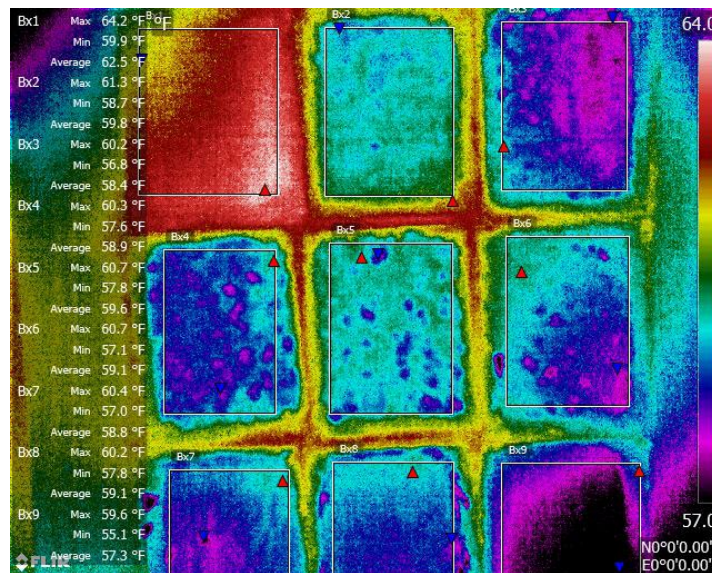


(a) $T_{\text{obj}} > T_{\text{refl}}$



(b) $T_{\text{obj}} < T_{\text{refl}}$

Figure 27. Picture and thermal image of soil samples



Additional Tests

To minimize the effects of uncontrolled reflected radiation sources, a new test setup was tried in this study. In this test setup, nine cans of soil sample with different moisture contents were arranged in a 3×3 array and placed inside a cardboard box with a hole cut in the box for the thermal camera to view through, as shown in Figure 28. Figure 29 shows that the measured apparent temperatures of soil samples with relative smooth and rough surfaces at different moisture content. A relative large decrease of measured apparent temperature is observed at low moisture contents and then a slight increase of measured apparent temperature is observed after a certain soil moisture content. The measured apparent temperature appears to be approaching a constant at high moisture contents. This may be because, when the soil moisture content is low, the thin water is mainly held in a film on the surface of soil particles, which decreases the soil's reflectivity. As the soil moisture content increases, the water starts filling the voids of soils and dominate the emissivity of the soil surface. It is also observed that the measured apparent temperatures are lower for rough surfaces, as compared to flat surfaces, indicating that rough surfaces increase the emissivity of the soil surface. The technicians confirmed that the soil surface roughness can be more consistent for soil on the dry side than on the wet side in the laboratory settings.

As shown in Figure 30, the results of additional tests also show that the measured apparent temperature is sensitive to the surface soil moisture content up to a certain depth. However, the current study did not delve too deeply into the determination of this depth.

Figure 28. Test setup with cardboard box



(a) Top View



(b) Inside View



(c) Flat surface



(d) Rough Surface

Figure 29. Apparent temperature vs moisture content with new test setup

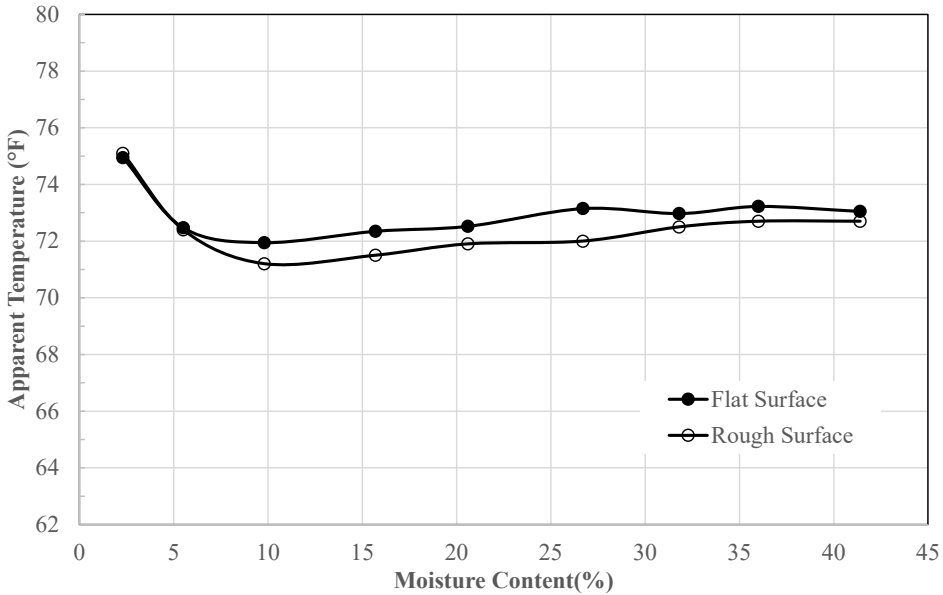
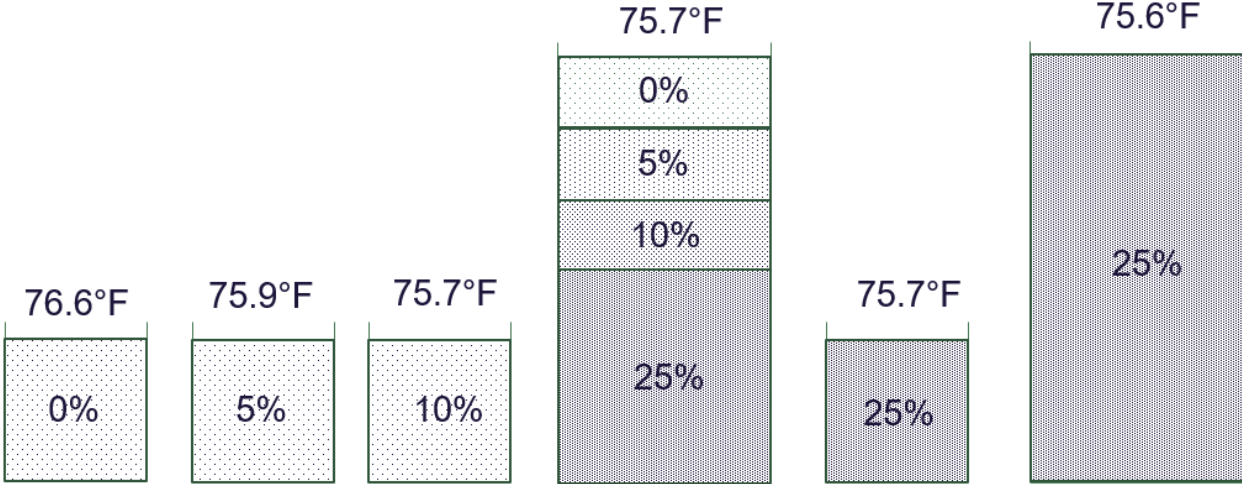


Figure 30. Impact of the soil below the surface on measured apparent temperatures



Field Testing at Pavement Research Facility Site

Flight sessions 1 and 2 are trial and error sessions. Therefore, only field testing results on the soil embankment at the PRF of LTRC for flight sessions 3, 4, and 5 are discussed here. One side of the embankment with a three-to-one slope was used to test the thermal camera and RedEdge multispectral camera during the field testing. Figure 31 to Figure 33 shows the slope that was wetted with different gallons of water in each zone. The white buckets with ice water in them in the photo served as ground control points for determining the locations of the different soil zones on the slope in the image.

Figure 31. Embankment soil with different moisture contents during flight session 3



Figure 32. Embankment soil with different moisture contents during flight session 4

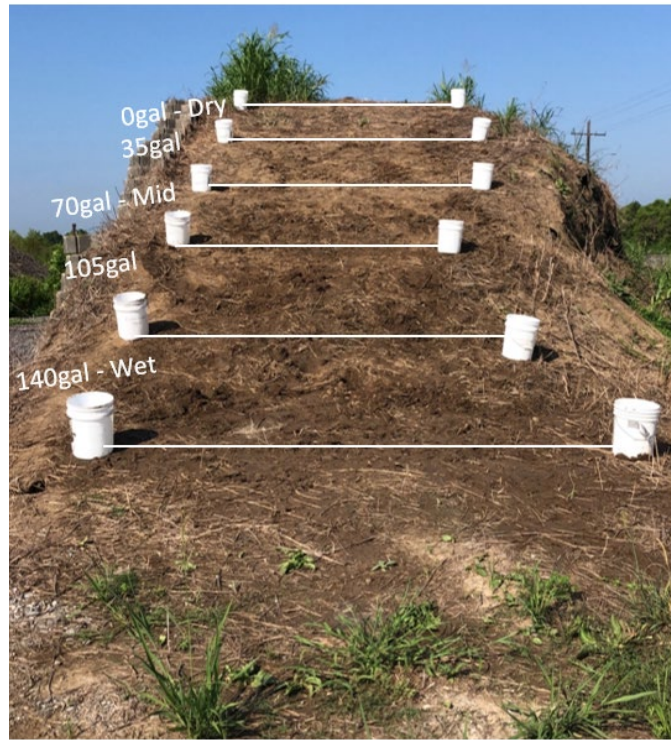
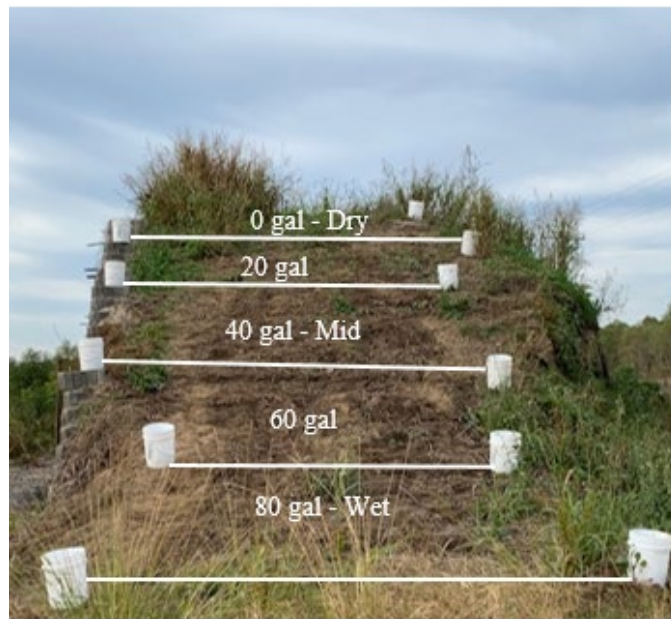


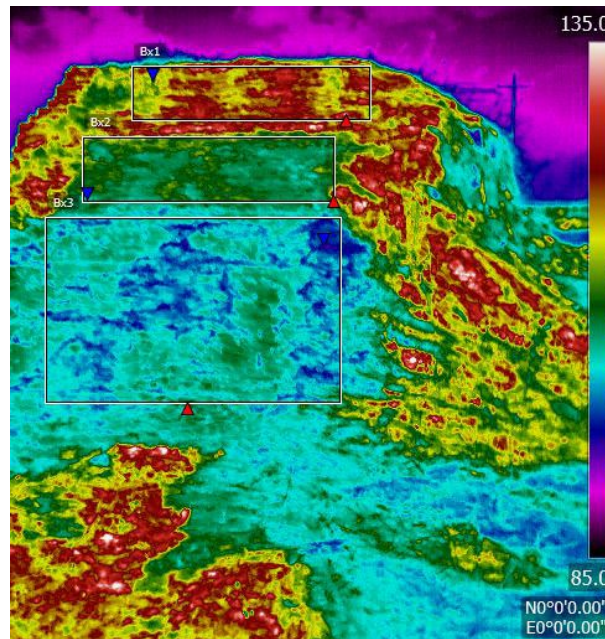
Figure 33. Embankment soil with different moisture contents during flight session 5



Thermal Camera

Figure 34 shows a typical thermal image, which was taken from ground. The image can tell the difference in soil moisture contents among different soil zones.

Figure 34. Thermal image of embankment soil slope taken from ground



Several drone flights were conducted the next day over the embankment at the PRF, and many thermal images were taken using the FLIR Vue Pro R camera. Figure 35 shows typical thermal images at different heights. It can be said from the image that the camera can detect the difference in moisture contents for the ground soil on the slope. The quality of the images for 300 ft. and 400 ft. is not as good as the ones from the height of 100 ft. and 200 ft. With limited soil moisture variations in the field, it is observed, as shown in Figure 36 to Figure 38, that the drier the soil, the higher the apparent temperature, which is different from what has been observed from the laboratory testing in this study. The variation is more significant when the soil is relative dry. It is also noted that the apparent soil surface temperatures are different for each flight session, especially for flight session 5. Considering the difference in the ambient environment among them, it can be concluded that the correlation between the soil moisture content and apparent temperature reading from the thermal camera is very complicated and only has a relative value for comparison.

It is also noted that the difference among different soil zones in thermal images taken during drone flights is not as clear as that in the thermal images taken from the ground. Height and angle may be some possible reasons with the different soil zones becoming less noticeable as the increase of the flight height. Also as mentioned earlier, the drone-based thermal images were taken a day after the soil was wetted, and different soil zones became almost indistinguishable because of the dried surface. This may indicate the importance of a time frame during which the images are taken. It also indicates that the sensing depth of thermal camera, i.e., the depth of the deepest soil that can be “seen” by a thermal camera, needs to be studied because the soil moisture content in subsurface varies with depth and can have an effect on thermal images.

Figure 35. Thermal images of embankment soil slope at different heights

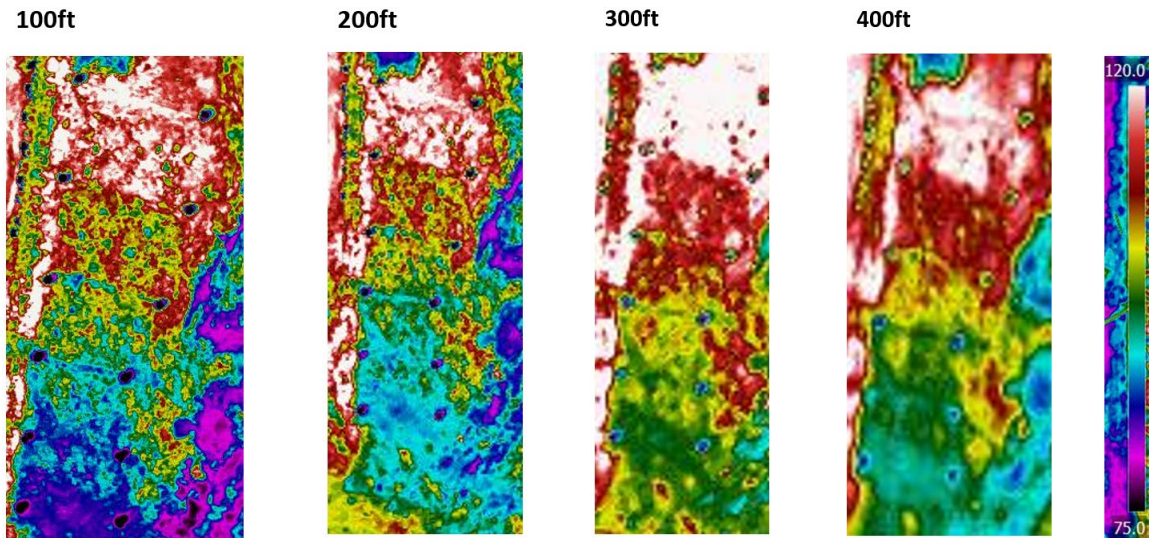


Figure 36. Variation of apparent soil surface temperature with moisture for flight session 3

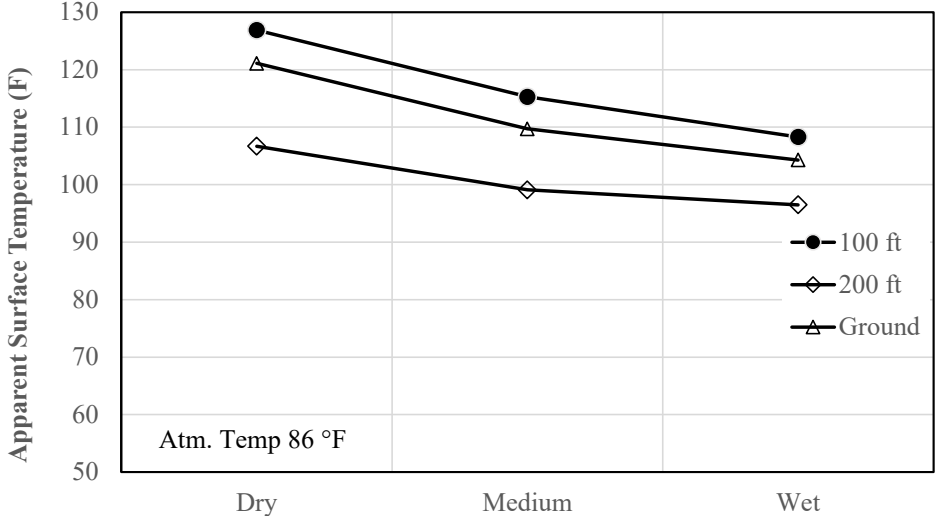


Figure 37. Variation of apparent soil surface temperature with moisture for flight session 4

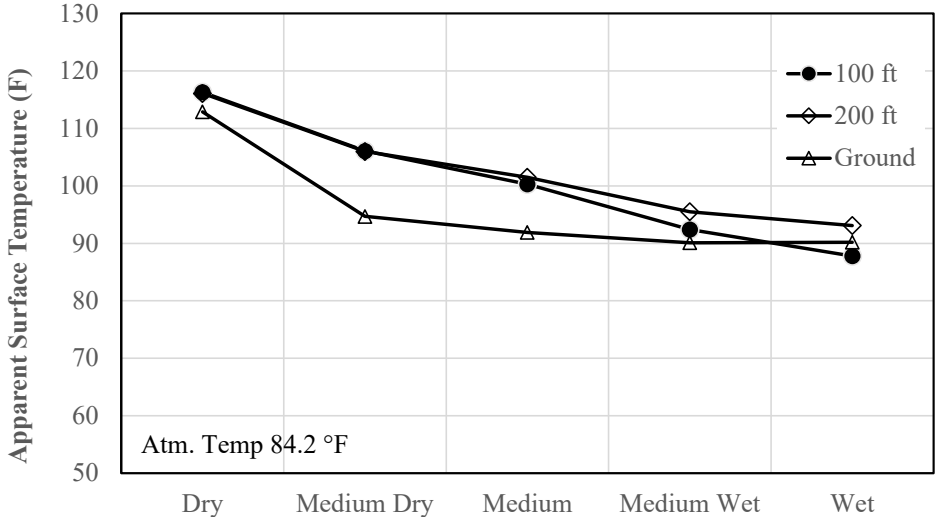
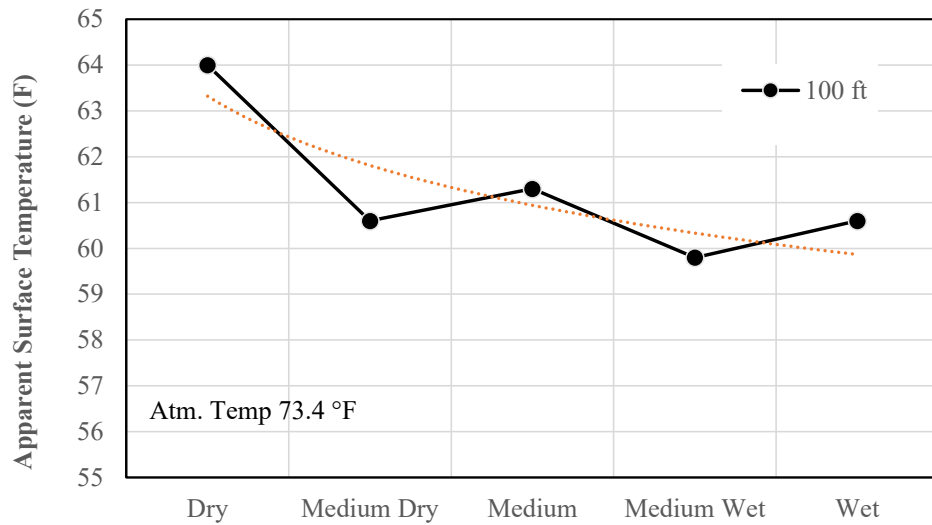


Figure 38. Variation of apparent soil surface temperature with moisture for flight session 5



During the processing of thermal images that we collected from the field, it took great pain and effort to locate the interested area out of hundreds of images, as shown in Figure 39. The research team tried printing out all images and manually put them together to create a overall image of the investigated area, as shown in Figure 40. However, due to color scheme differences of each image, this is not a easy task.

Figure 39. Interested area search

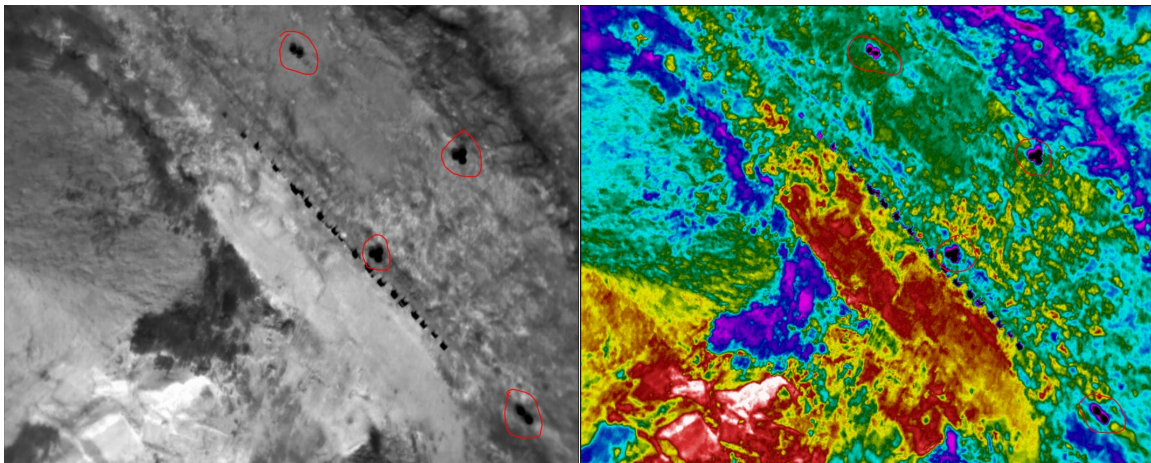


Figure 40. Manually stitched images



After a series of trial and error, it was realized that the best way to overcome this hurdle was to stitch all images together to create a thermal map. To do this, a way to inject the GPS data into the images had to be determined. A stand-alone geotagging module by sUAS, as shown in Figure 41, was able to be used together with FLIR Vue Pro for geotagging thermal images. It was tested during Flight session 4 but failed to capture any thermal images due to a battery issue. This geotagger has to be powered by its own battery. After solving the battery issue, it was tested again during Flight session 5 and successfully collected thermal images with GPS information embedded. Now, another issue arose: how to stitch the collected thermal images together. FLIR Tools does not have this function, so the team had to turn to ArcGIS Drone2Map and ArcGIS Pro to help stitch the thermal images. Both softwares are available for DOTD users. Maps were successfully created by using both softwares, as shown in Figure 42, but new issues emerged. When the team exported the maps and loaded them back into FLIR Tools, it was discovered that all the radiometric information in the original thermal images was lost. After reaching out to Drone2Map and ArcGIS Pro development team, the team was informed that they noted the problem and would work on implementing a solution to retain the radiometric information on the thermal data during processing.

Figure 41. Geotagger by sUAS

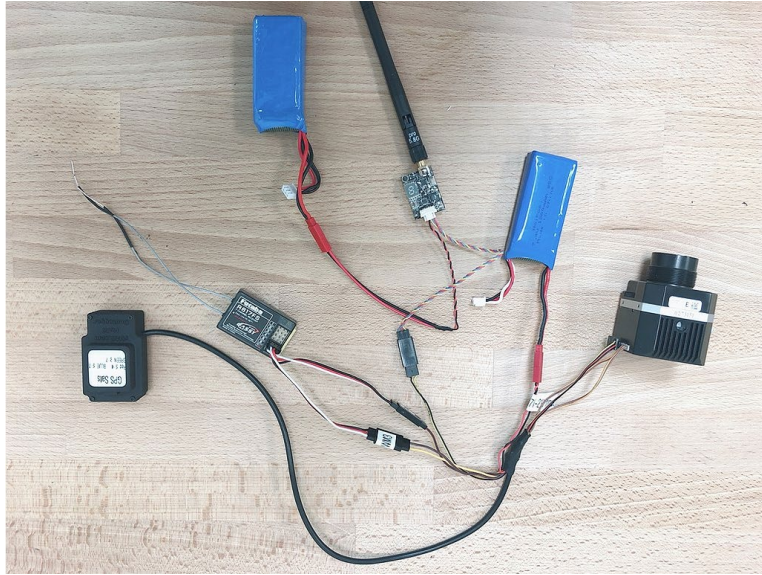
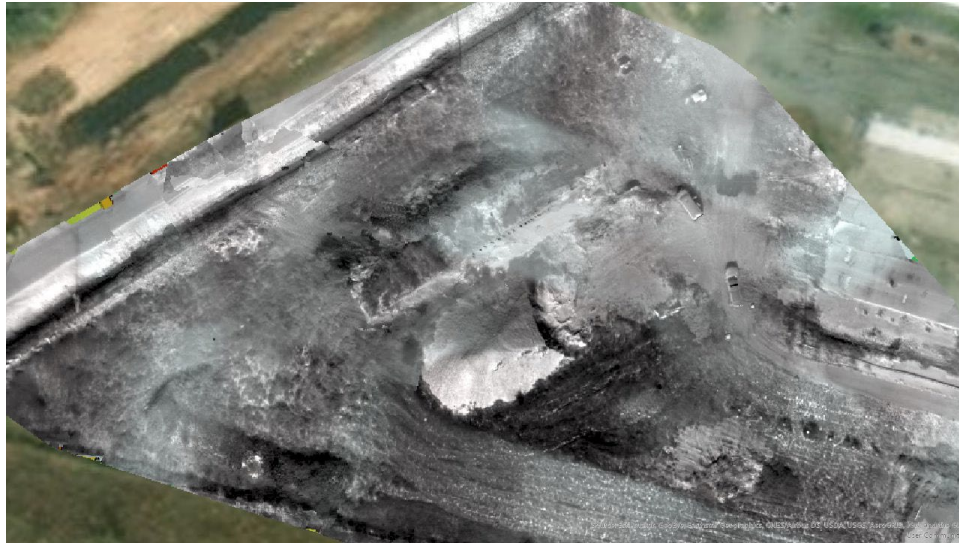


Figure 42. Thermal map for PRF site



RedEdge Camera

Figure 43 shows a typical RedEdge camera orthomosaic map created by Drone2Map. Figure 44 displays the raw unprocessed image of each band. It is evident that vegetation absorbs more red and blue light and reflects more green, rededge, and near infrared (NIR). The image can distinguish variations in soil moisture contents among different soil zones due to slight color difference. With limited soil moisture variations in the field, it is observed, as depicted in Figure

45 to Figure 47, that the drier the soil, the higher the pixel values for all five bands. This indicates that water decreases the soil's reflectivity in this study, i.e., dry soil in this study becomes darker in color when water is added to it. The color of the dry soil depends on what little particles comprise it—specifically what minerals it contains. When water replaces the naturally occurring oxygen in the soil it darkens.

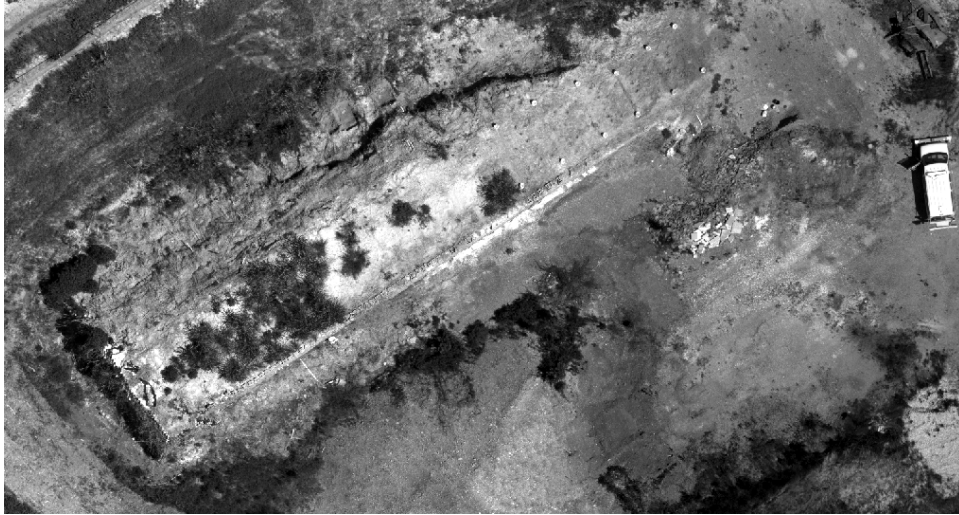
The combination of reflectivity measurement with different spectral bands, such as NDVI and GNDVI, are also explored here to see if any correlation exists between these indices and soil moisture.

The variation of NDVI with soil moisture is presented in Figure 48, while variation of GNDVI with soil moisture is shown in Figure 49. As observed in the Figures, there is no consistent trend between NDVI/GNDVI and soil moisture. It would be interesting to explore more electromagnetic spectral bands in future to determine which band or combination of bands is more sensitive to the combined effects soil and moisture. Hyperspectral imagery could be a viable option for further investigation.

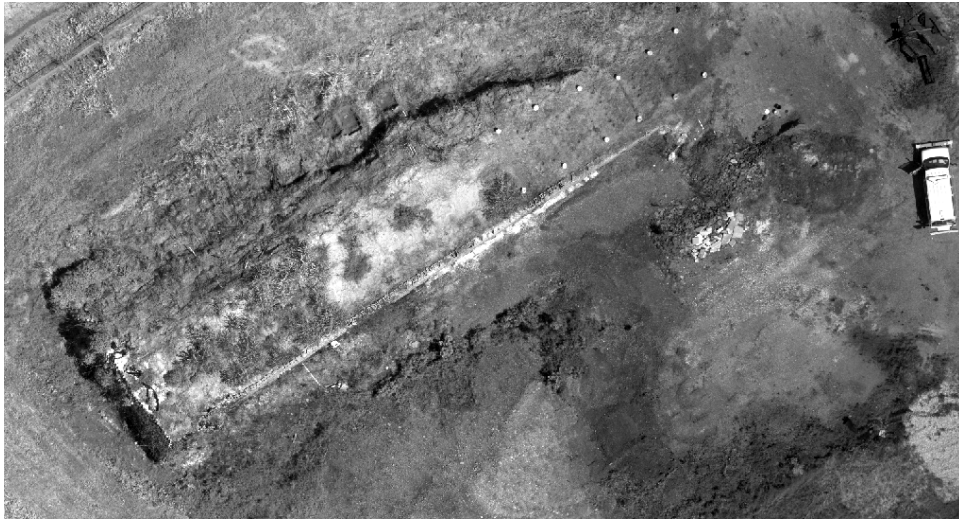
Figure 43. Orthomosaic map for PRF site



Figure 44. Raw image of individual band



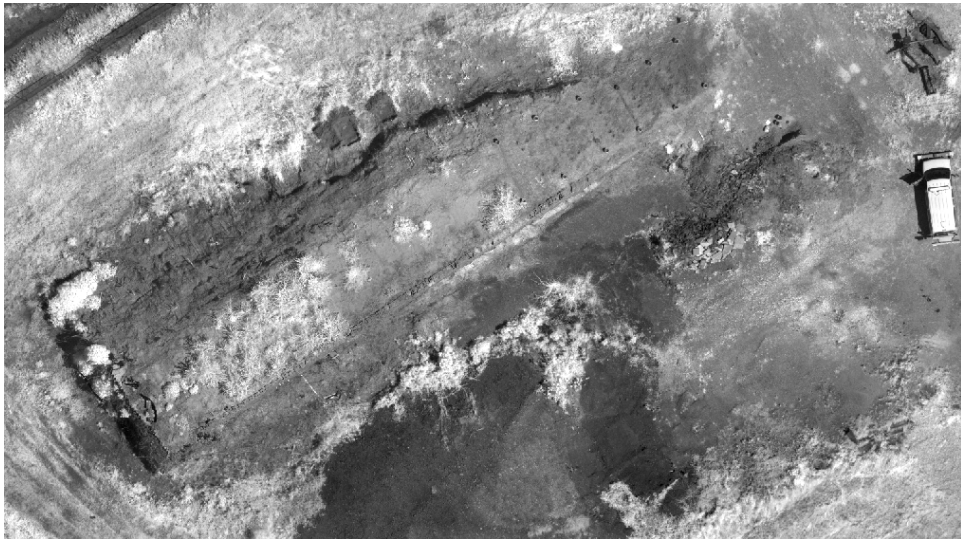
(a) Red Band



(b) Green Band



(c) Blue Band

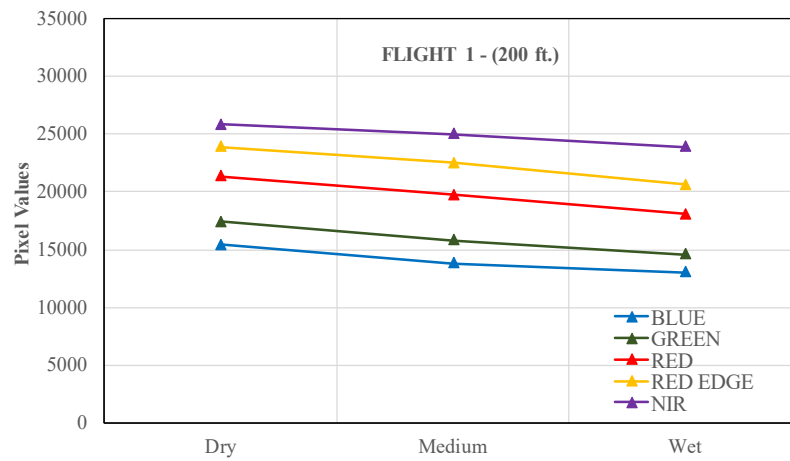


(d) NIR Band

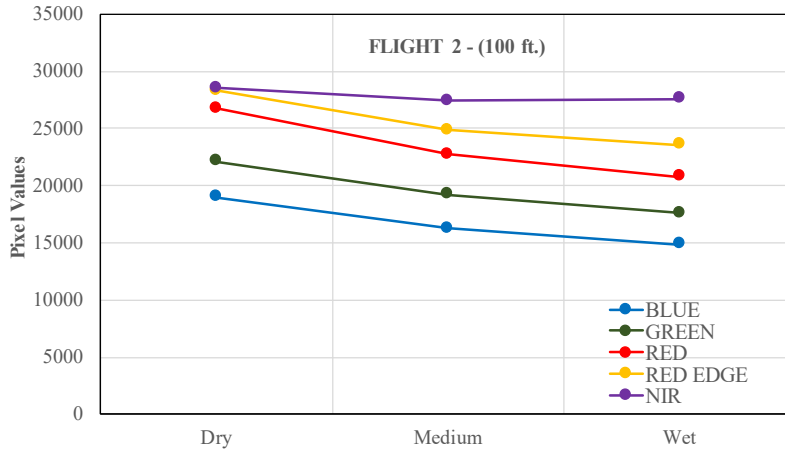


(e) Rededge Band

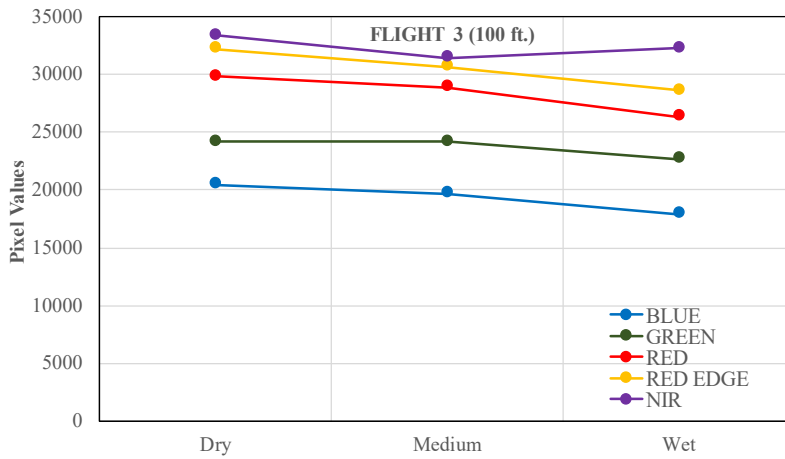
Figure 45. Spectral profile for flight session 3



(a) Flight 1 at 200 ft.

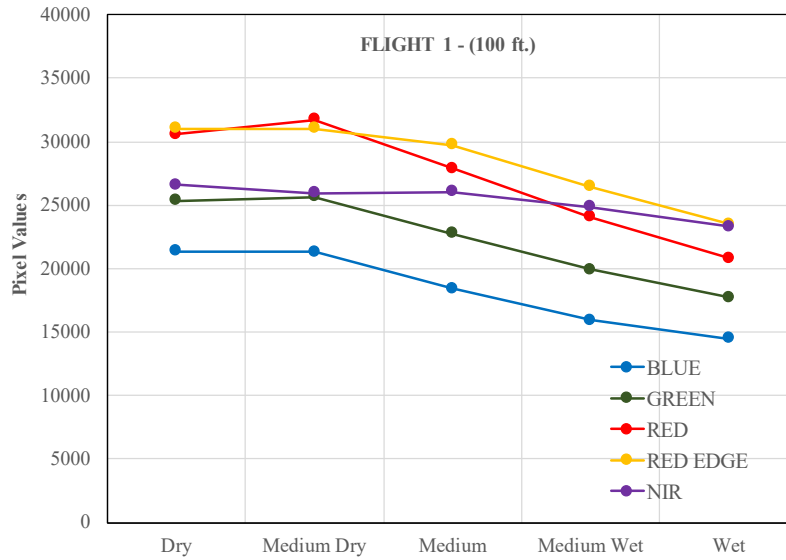


(b) Flight 2 at 100 ft.

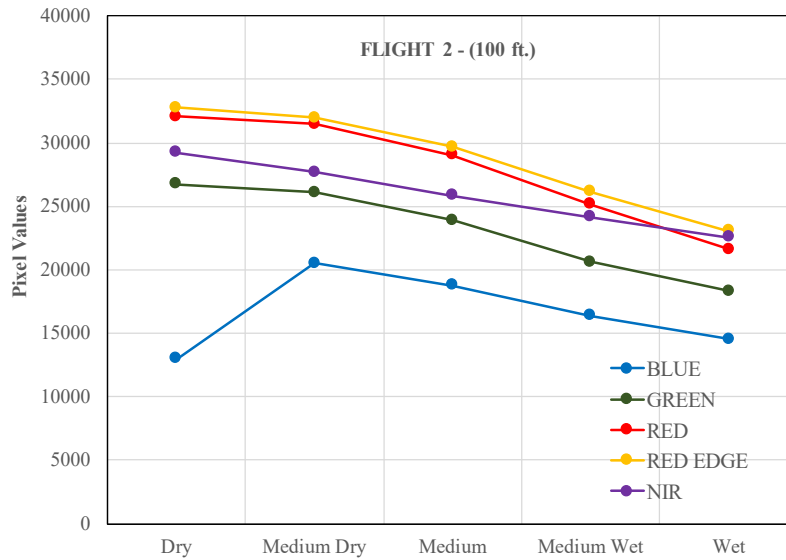


(c) Flight 3 at 100 ft.

Figure 46. Spectral profile for flight session 4

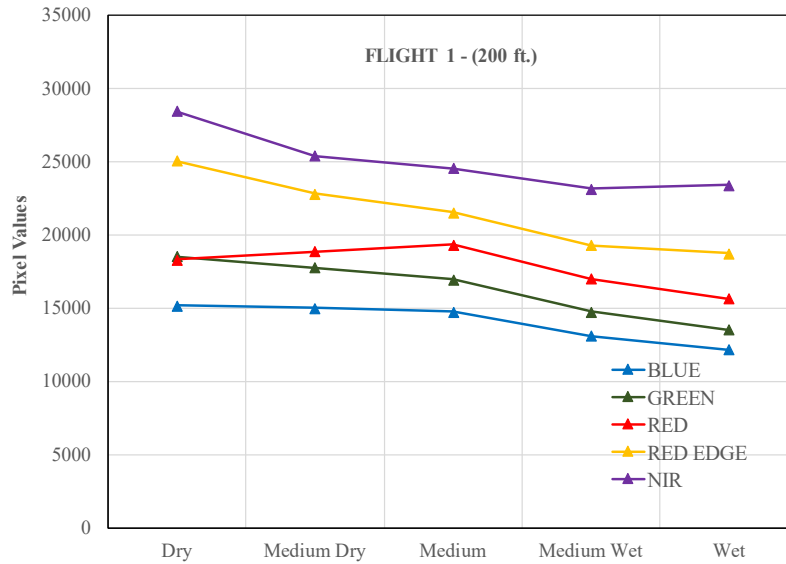


(a) Flight 1 at 100 ft.

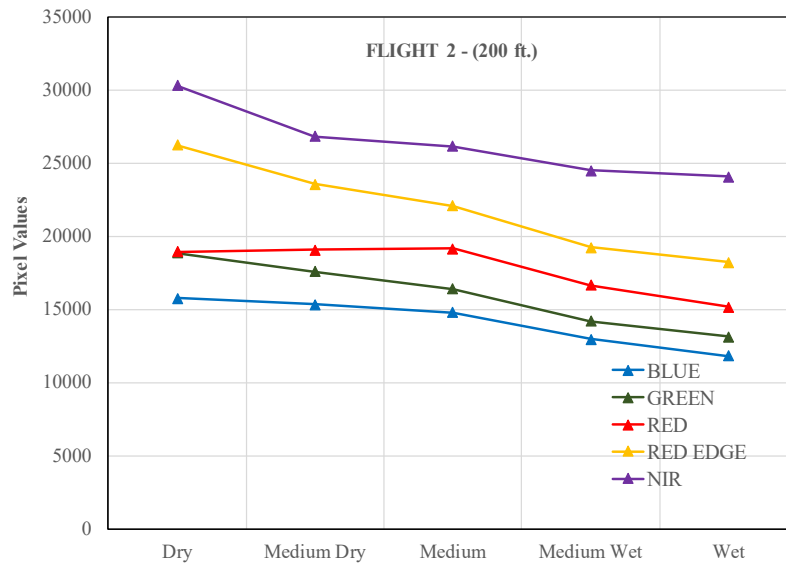


(b) Flight 2 at 100 ft.

Figure 47. Spectral profile for flight session 5

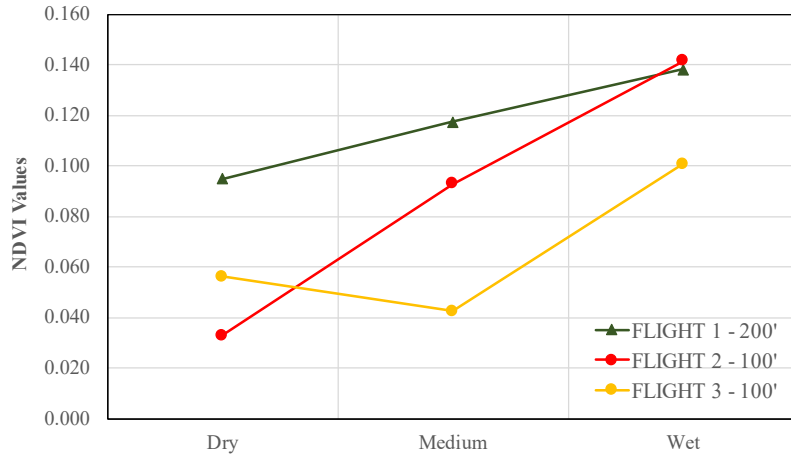


(a) Flight 1 at 200 ft.

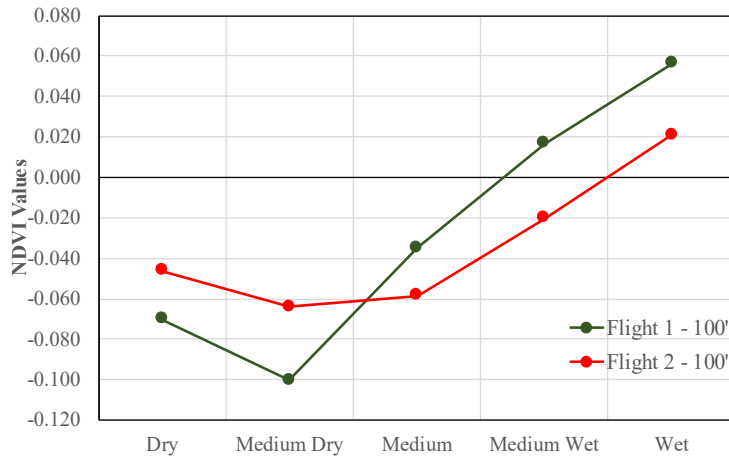


(b) Flight 2 at 200 ft.

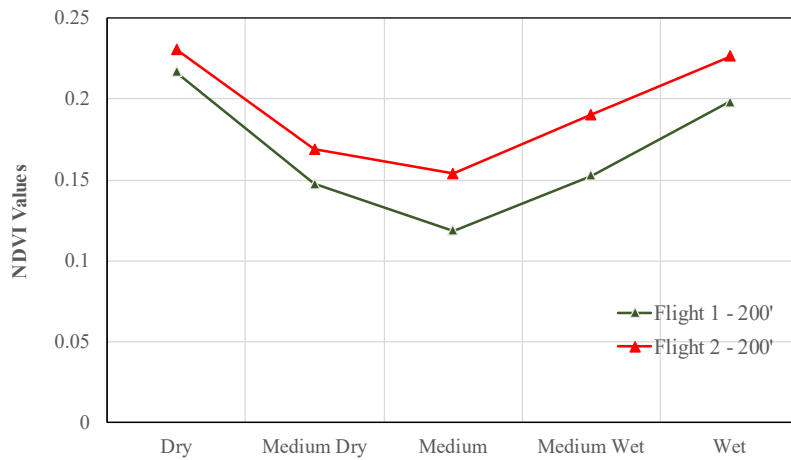
Figure 48. NDVI profile



(a) Flight Session 3

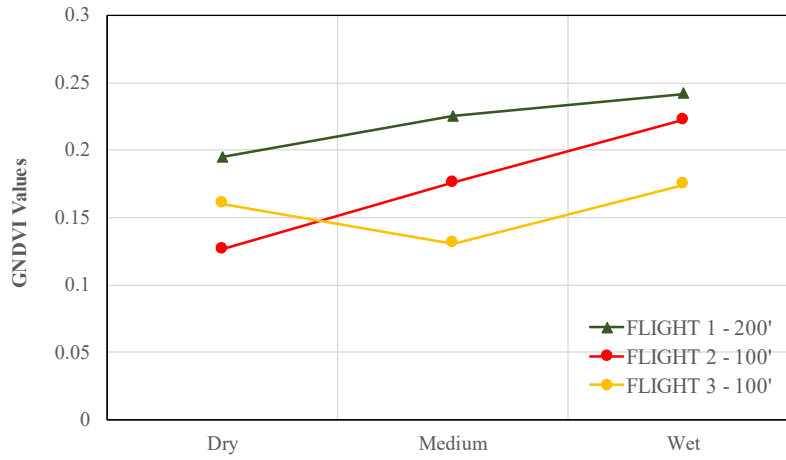


(b) Flight Session 4

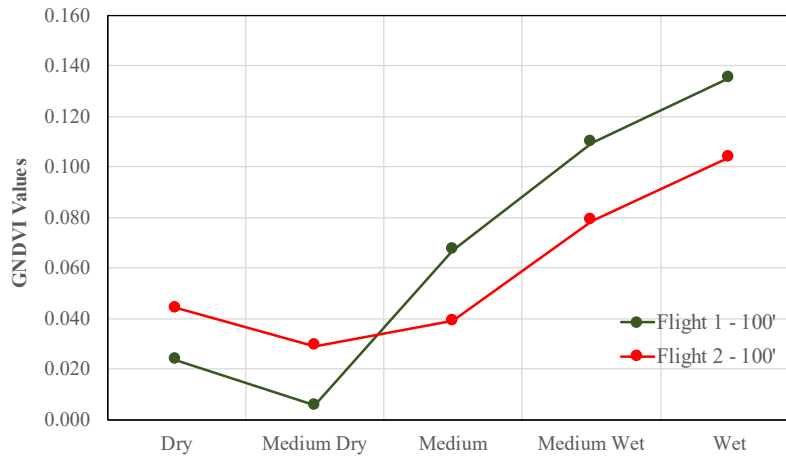


(c) Flight Session 5

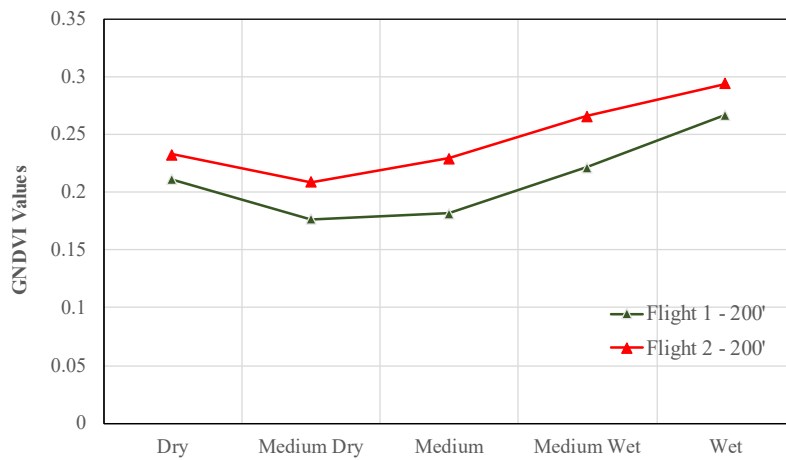
Figure 49. GNDVI profile



(a) Flight Session 3



(b) Flight Session 4



(c) Flight Session 5

Field Testing at I-10 @ LA30 Embankment Site

Both multispectral RedEdge camera and thermal camera were brought to the field for capturing image data on March 3, 2021. It was a sunny day with the temperature of 55°F (13°C). The day chosen for data collection was a day or two after rain, so the surface water would be trapped in cracks, soaking the adjacent soil and potentially creating a wetter area near the cracks. The flight height was 200 ft. Figure 50 shows a typical RedEdge camera orthomosaic map created by Drone2Map. Figure 51 shows the raw unprocessed image of each band. The failure area does not stand out in these images because of vegetation. Figure 52 shows a thermal image near the failure area. Apparent temperature profiles cross the slope at the failure area are shown in Figure 53. Temperature dips were observed at both the failure area and ditch area. Figure 54 presents a close view of orthomosaic map near the failure area. NDVI profiles were plotted in Figure 55, and nothing special was observed at the failure area. A suspicious area, presented in Figure 56, was also observed when we went through all thermal images. The apparent temperature profile cross the slope at this location shows an apparent temperature dip (Figure 57). A close view of the orthomosaic map near the suspicious area is shown in Figure 58. A high NDVI value in the NDVI profile at this location (Figure 59) indicated that this area was greener. Field visit confirmed that this area has tall and green grass.

This observation prompted the researchers to explore new ways to interpret data. The temperature vegetation dryness index (TVDI) is an index developed to empirically interpret the water stress associated with land surface temperature and vegetation within the NDVI/LST space. By plotting all data in the NDVI/LST space, as shown in Figure 60, it is clearly demonstrated that the failure area and ditch area are close to the wet edge, which means high moisture content. The suspicious tall grass area falls into the middle between the dry edge and wet edge. It seems that TVDI is capable of identifying the dry and wet areas, even with vegetation. It should be pointed out here that the NDVI value and apparent surface temperature plotted in pairs were hand-picked by eyes and may not be from exact same location. This process can be much better handled by creating thermal and NDVI maps and then automatically pairing each point from both maps based on GPS coordinates. However, this would require the coordination of efforts by researchers as well as software developers. Currently, we do not have this capability.

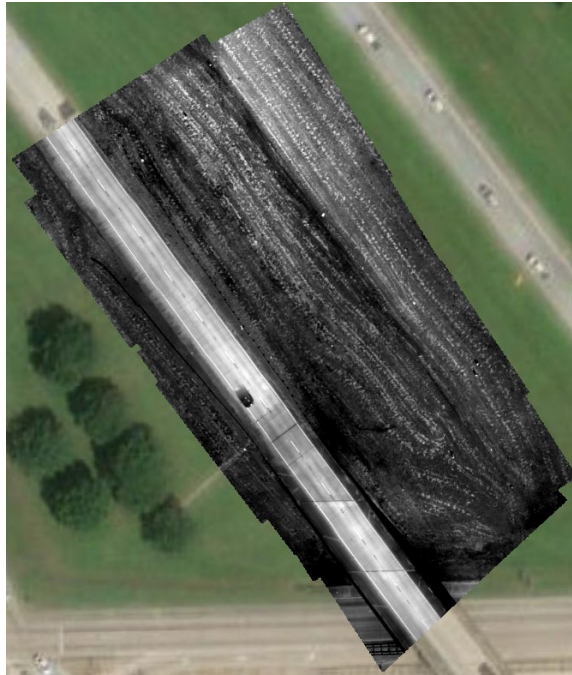
In 2022, ESRI released a newer version of Drone2Map (Drone2Map 2022.1), which added thermal processing capabilities with radiometric JPEG support. Considering the fact that it is difficult to differentiate different soil moisture zones from current thermal images created using FLIR Tools as shown in Figure 36 and Figure 52, the researchers explored the newer version of

Drone2Map to better present the data. Figure 61 presents the thermal map of Gonzales embankment created using this newer version of Drone2Map with different display control strategies. Figure 61a uses the “stretch” symbology, which stretches the thermal readings along a color ramp. This is often used to eliminate extreme high and low values that represent noise in imagery. Figure 61b-e uses the “discrete” symbology, which groups the thermal readings based on a selected number of colors. Figure 61f-i uses the “classify” symbology, which assigns a color for each group of thermal readings. The break points between each group can be edited. It is observed that the display control strategy using “classify” symbology gives the best results. The failure area, ditch area, and suspicious area stand out more clearly in the images using “classify” symbology with the number of classes being five or less.

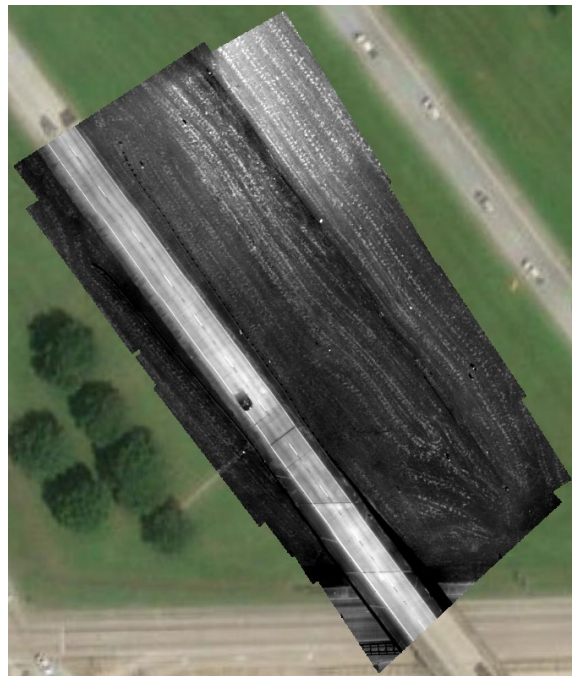
Figure 50. Orthomosaic map for I-10 @ LA30 embankment



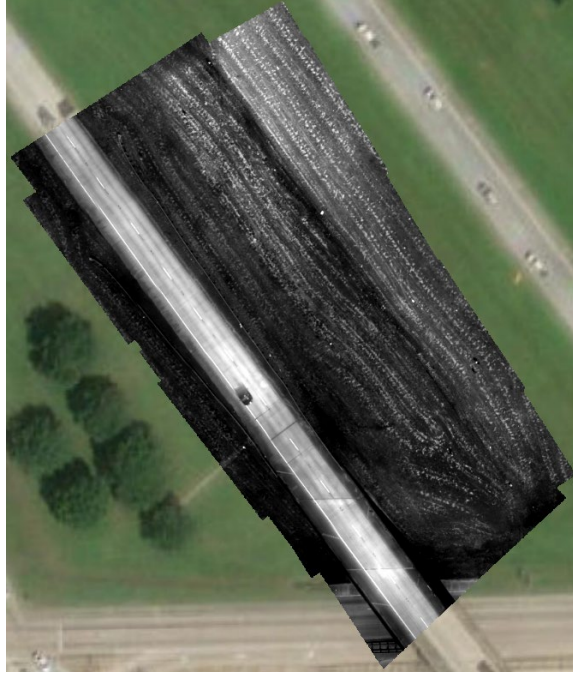
Figure 51. Raw image of individual band for I-10 @ LA30 embankment



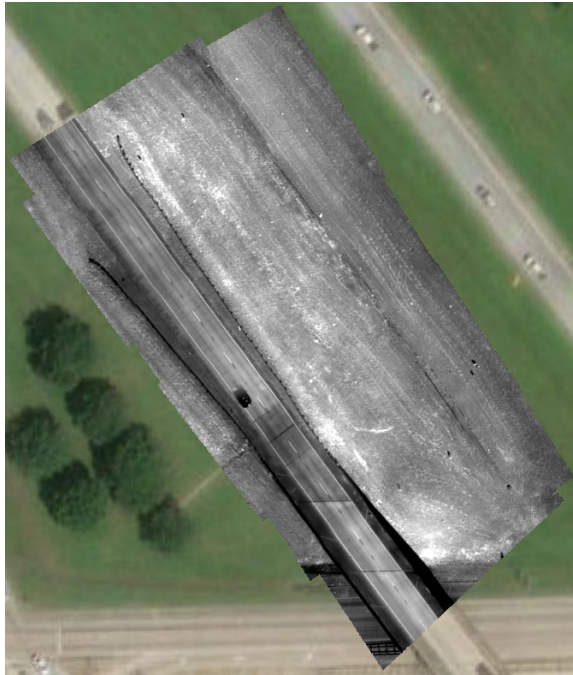
(a) Red Band



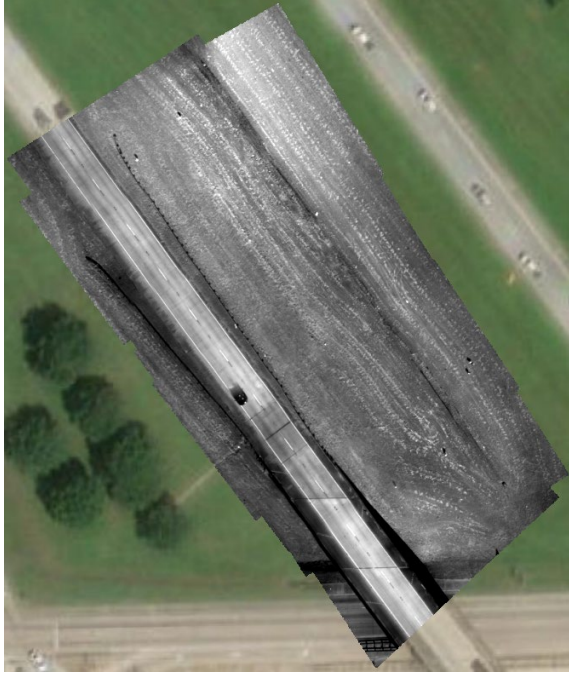
(b) Green Band



(c) Blue Band



(d) NIR Band



(e) RedEdge Band

Figure 52. Thermal image near the failure aArea for I-10 @ LA30 embankment

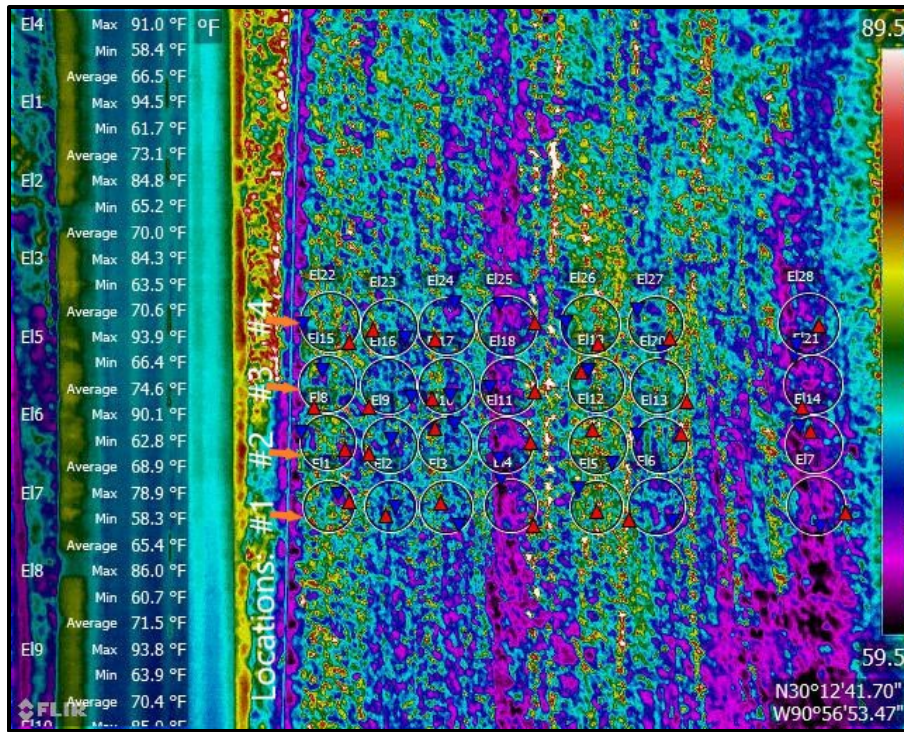


Figure 53. Apparent temperature profile across I-10 @ LA30 embankment near the failure area

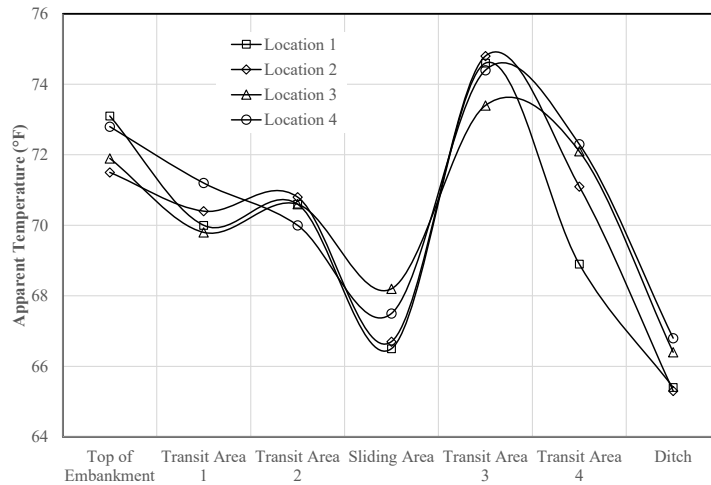


Figure 54. Orthomosaic map near the failure area for I-10 @ LA30 embankment



Figure 55. NDVI profile across I-10 @ LA30 embankment near the failure area

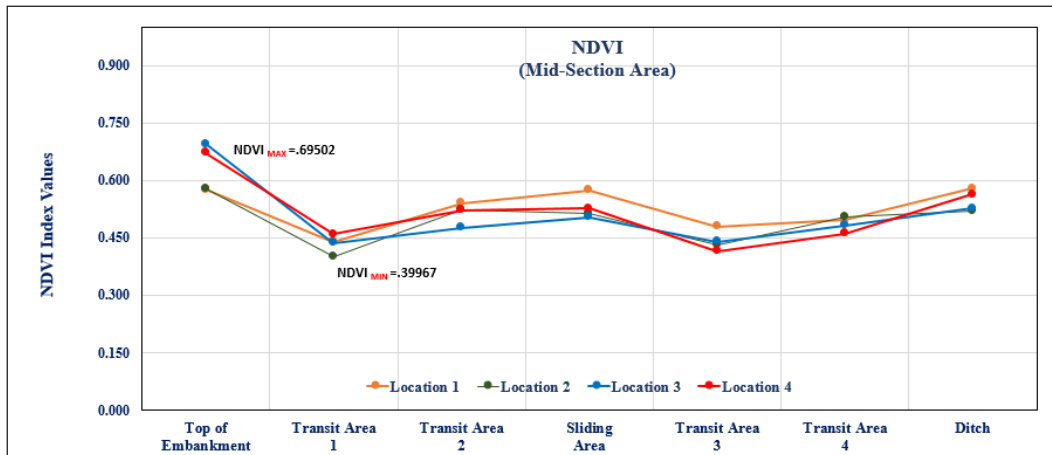


Figure 56. Thermal image near the suspicious area for I-10 @ LA30 embankment

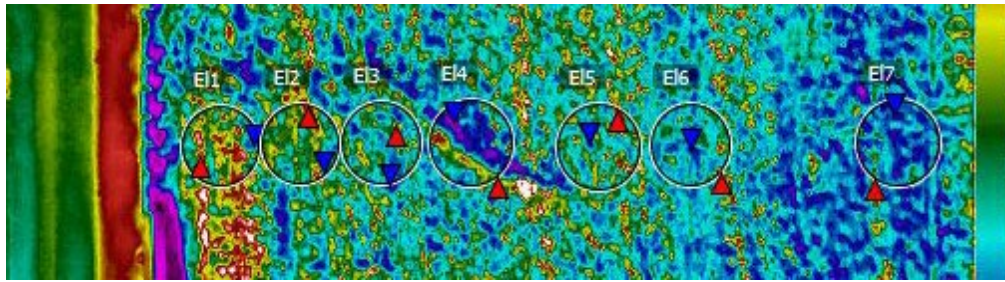


Figure 57. Apparent temperature profile across I-10 @ LA30 embankment near the suspicious area

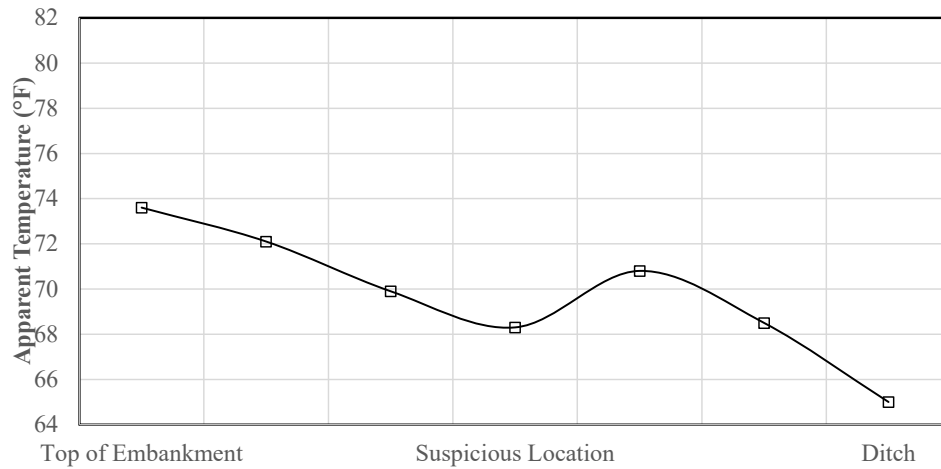


Figure 58. Orthomosaic map near the suspicious area for I-10 @ LA30 embankment



Figure 59. NDVI profile across I-10 @ LA30 embankment near the suspicious area

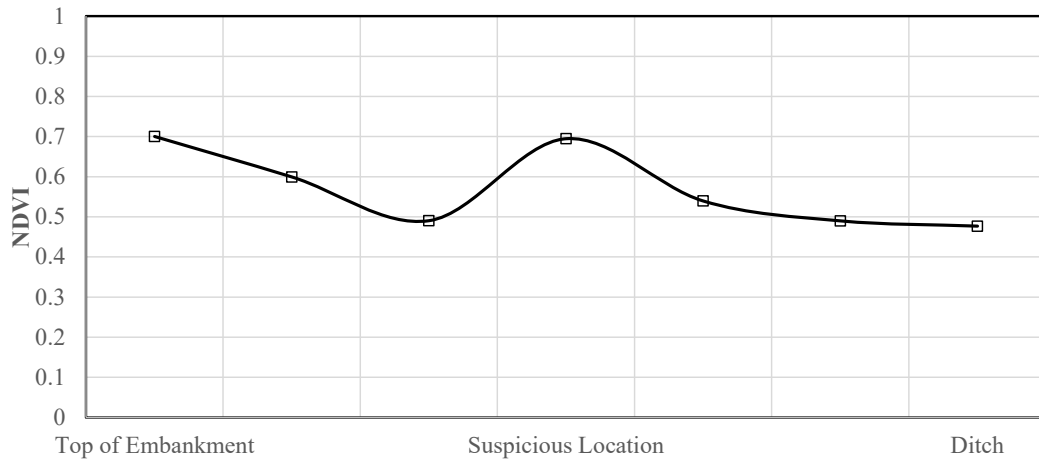


Figure 60. Scatterplots of Surface temperature and NDVI

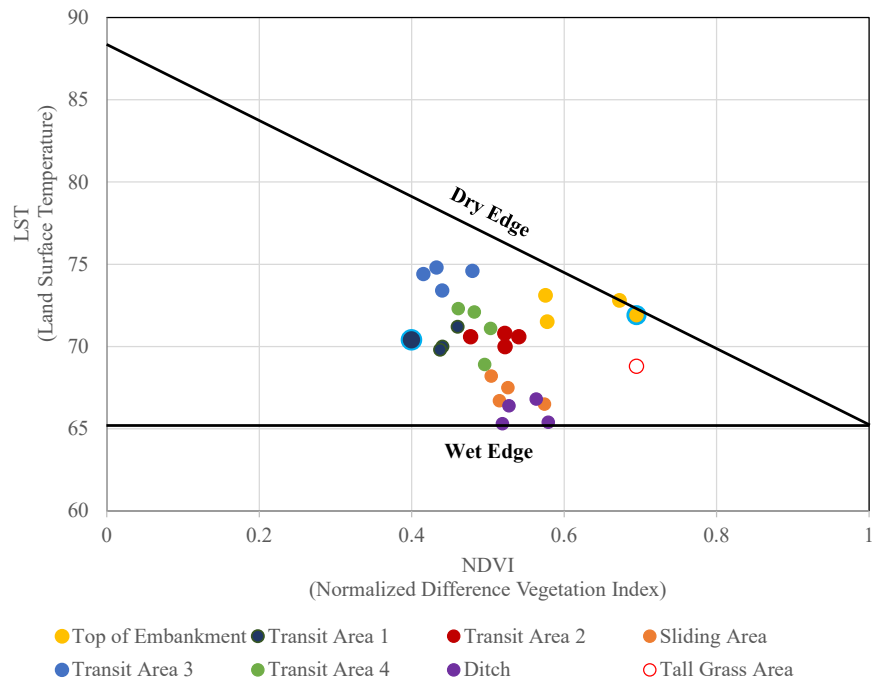
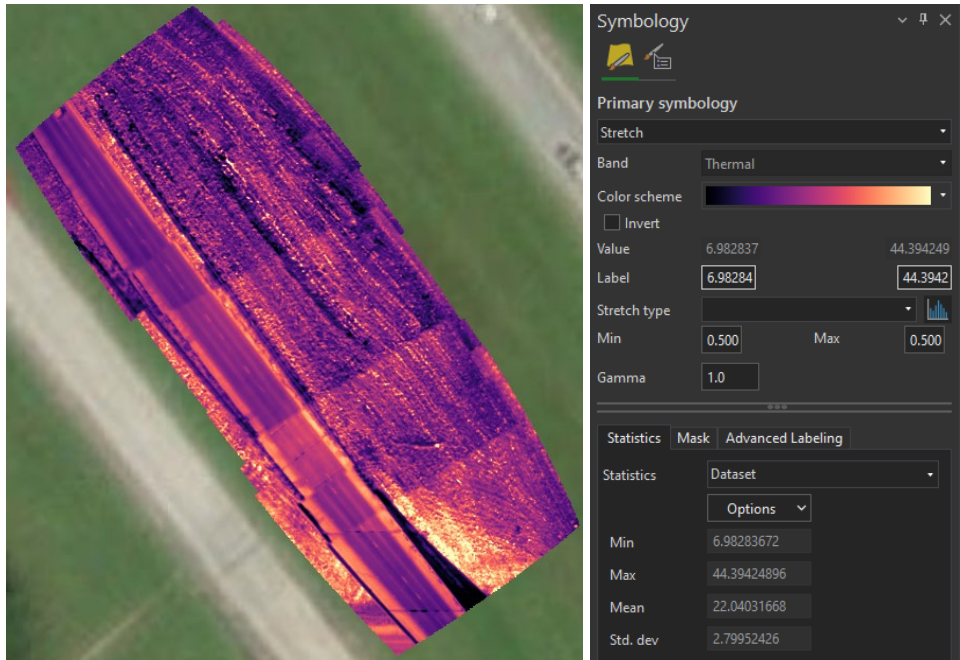
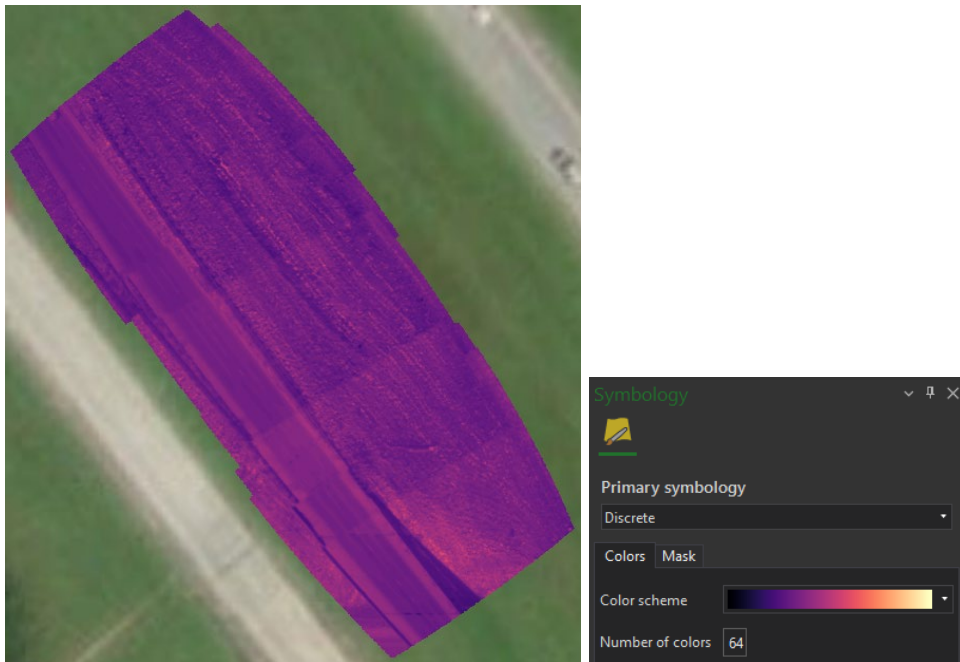


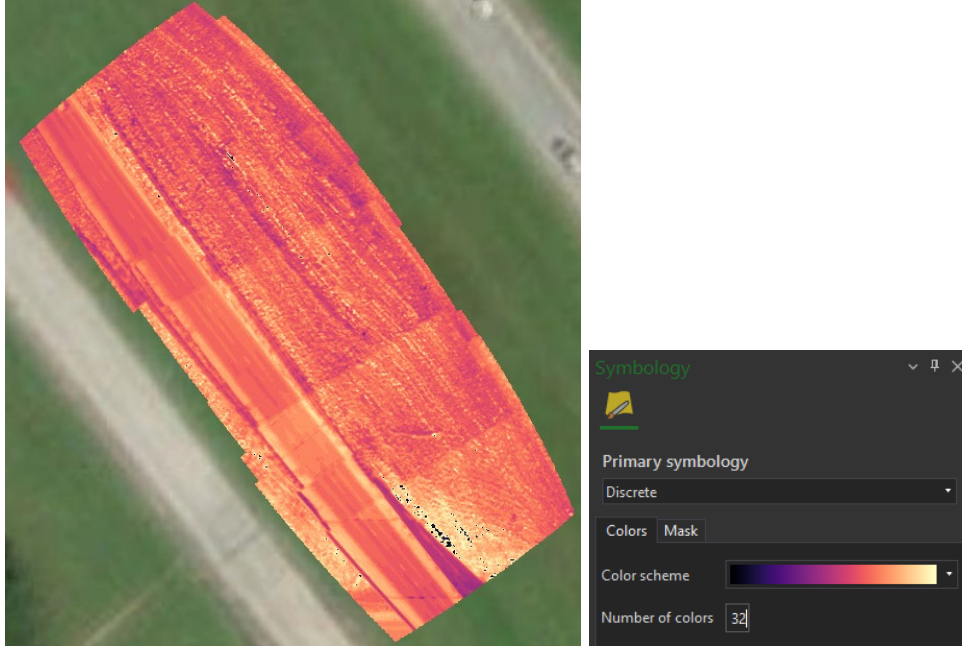
Figure 61. Thermal map of I-10 @ LA30 embankment



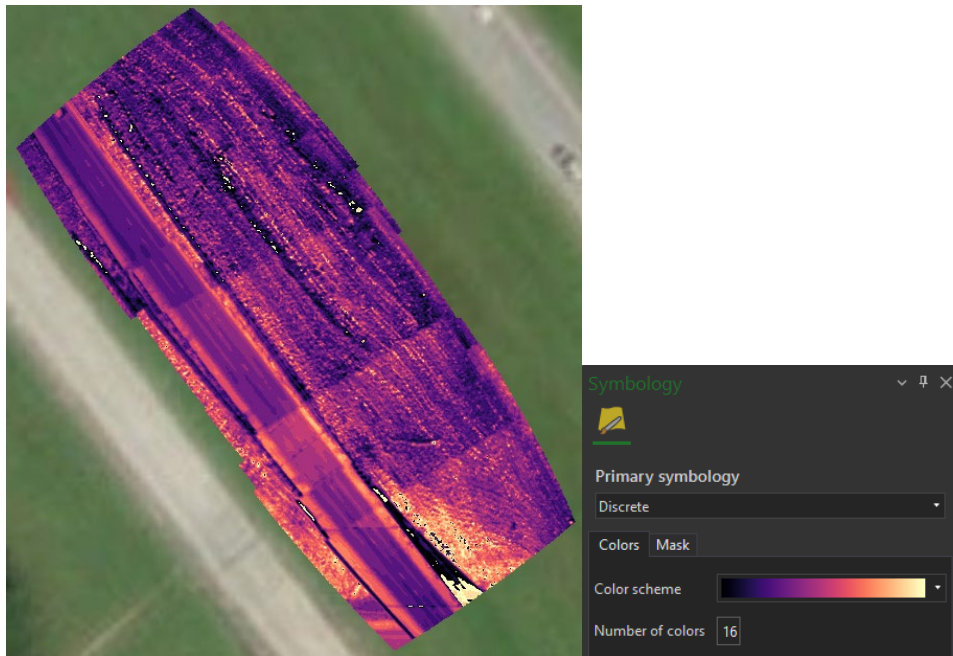
(a) Stretch



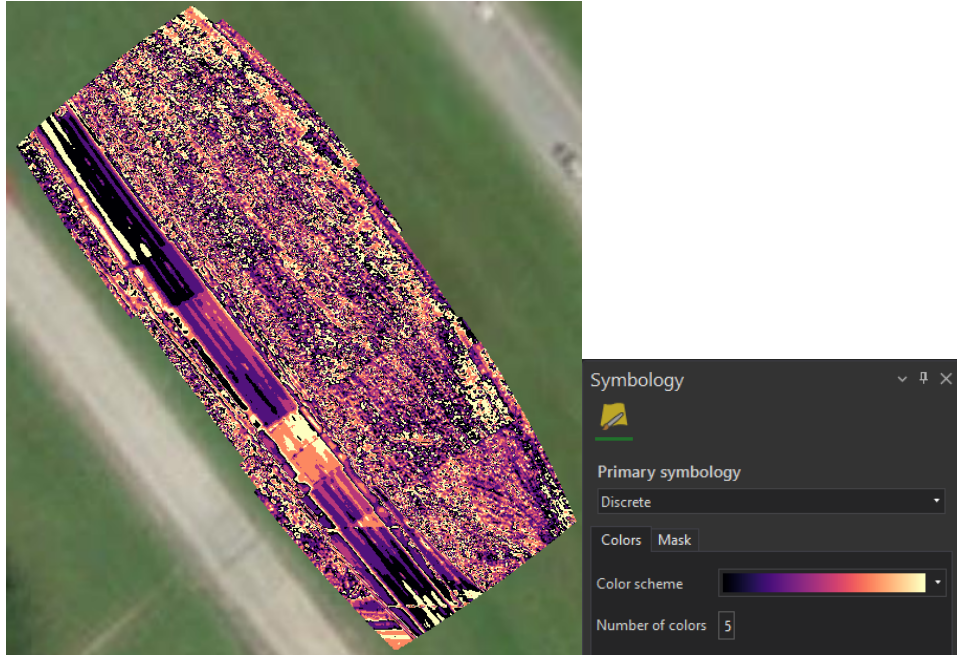
(b) Discrete with 64 colors



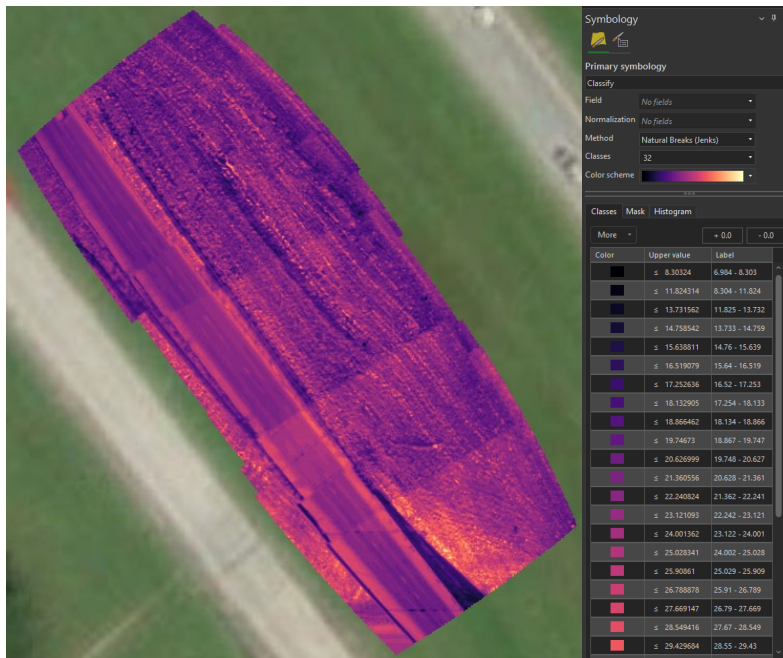
(c) Discrete with 32 colors



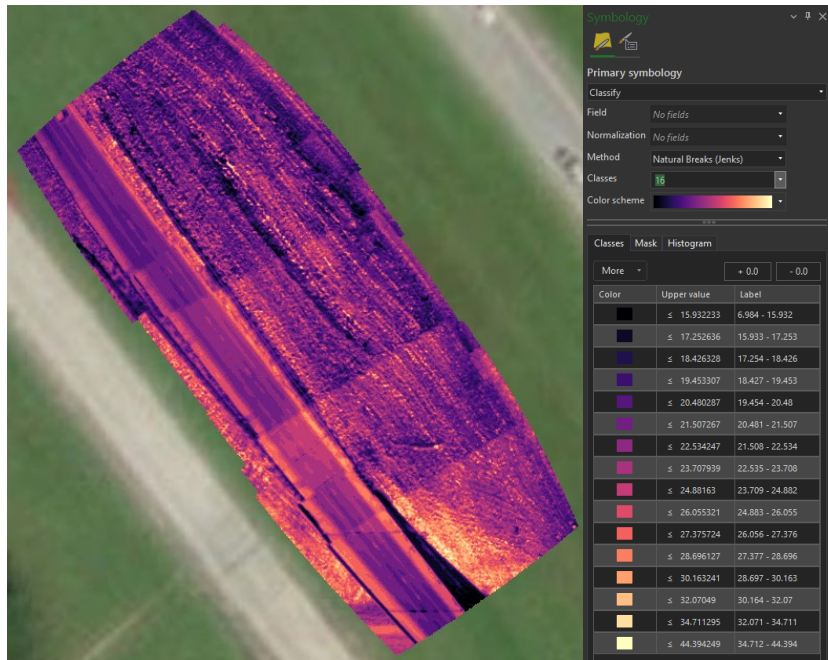
(d) Discrete with 16 colors



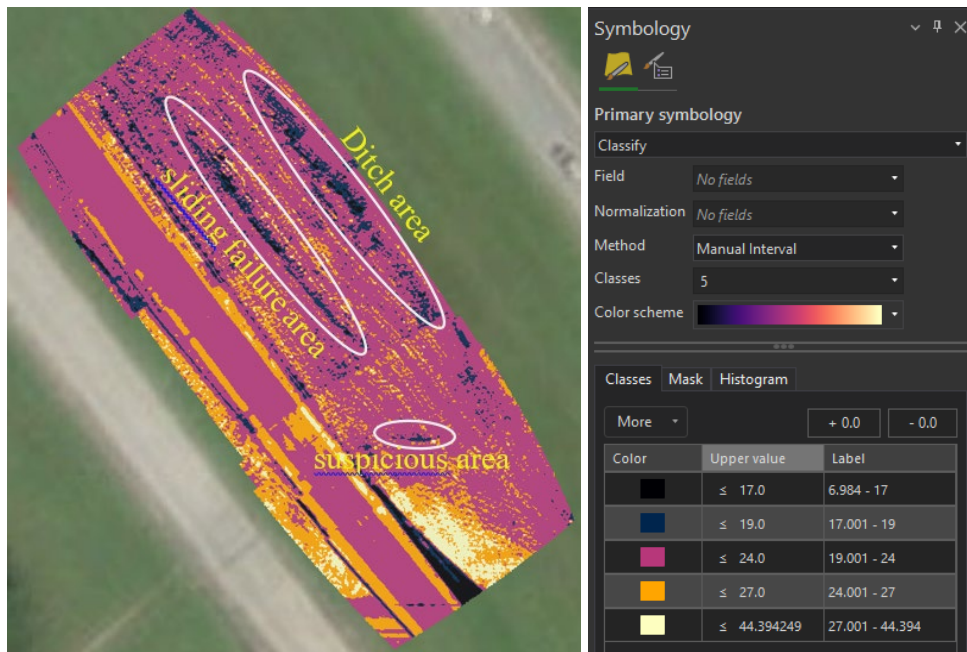
(e) Discrete with 5 colors



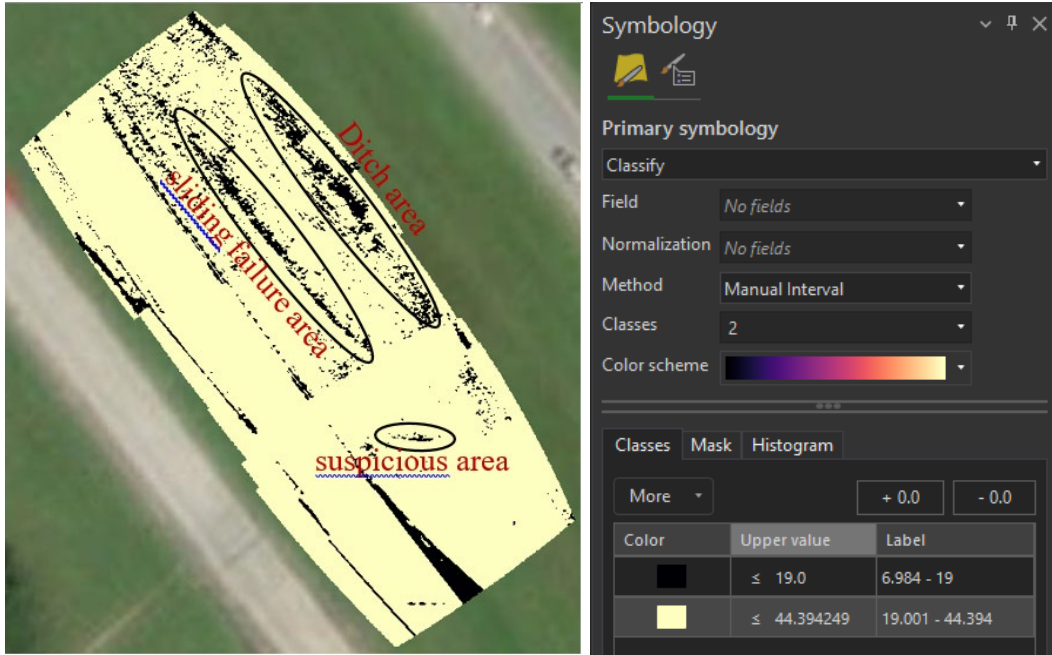
(f) Classify with 32 classes



(g) Classify with 16 classes



(h) Classify with 5 classes



(i) Classify with 2 classes

Field Testing at Iatt Lake Dam Site

Both multispectral RedEdge camera and thermal camera were brought to Iatt Lake Dam site for capturing image data on January 6, 2022. It was a cloudy and windy day with the temperature of 63°F (16°C). The flight height was 200 ft. A typical orthomosaic map of Iatt Lake dam captured by RedEdge camera was presented in Figure 62. Figure 63 shows the raw unprocessed image of each band. Nothing stands out in these images. Figure 64 presents the thermal map created using Drone2Map 2022.1 using “classify” symbology with the number of classes being six or less. (in black/dark blue color). Since open water of the Iatt Lake was captured in the images and was much cooler than the land surface, a separate class was created for the water body only. A couple of low thermal reading areas stand out in the images. Ground visual inspection on these areas did not notice any abnormal soil moisture. It must be pointed out here that vegetation hindered researchers' ability to see everything with their eyes. It is interesting to note that a sliding failure occurred/was discovered by researchers in one of those lower thermal reading areas, as shown in red circle in both thermal maps. Figure 65 presents a close view of the sliding failure area. This indicates that the thermal camera may be able to detect moisture difference that is hard to see by visual inspection. This would give the thermal camera a great potential in supplementing traditional visual highway embankment and dam inspections.

Figure 62. Orthomosaic map for Iatt Lake Dam



Figure 63. Raw image of individual band for Iatt Lake Dam



(a) Red Band



(b) Green Band



(c) Blue Band

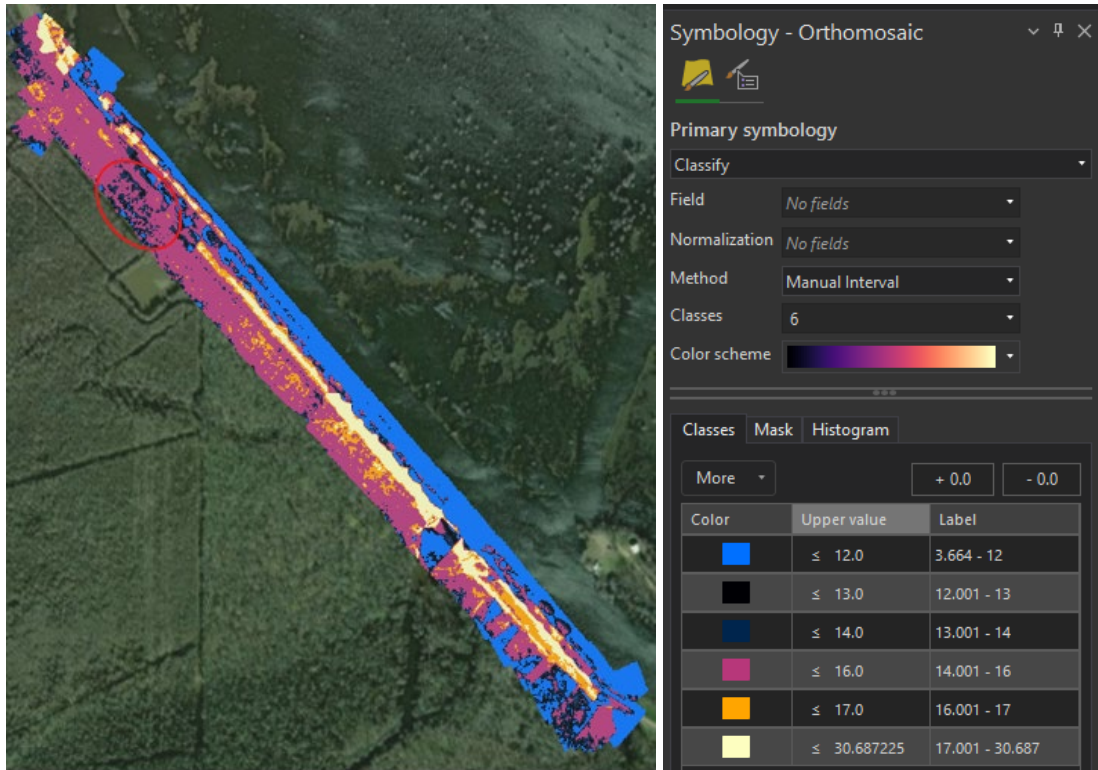


(d) NIR Band

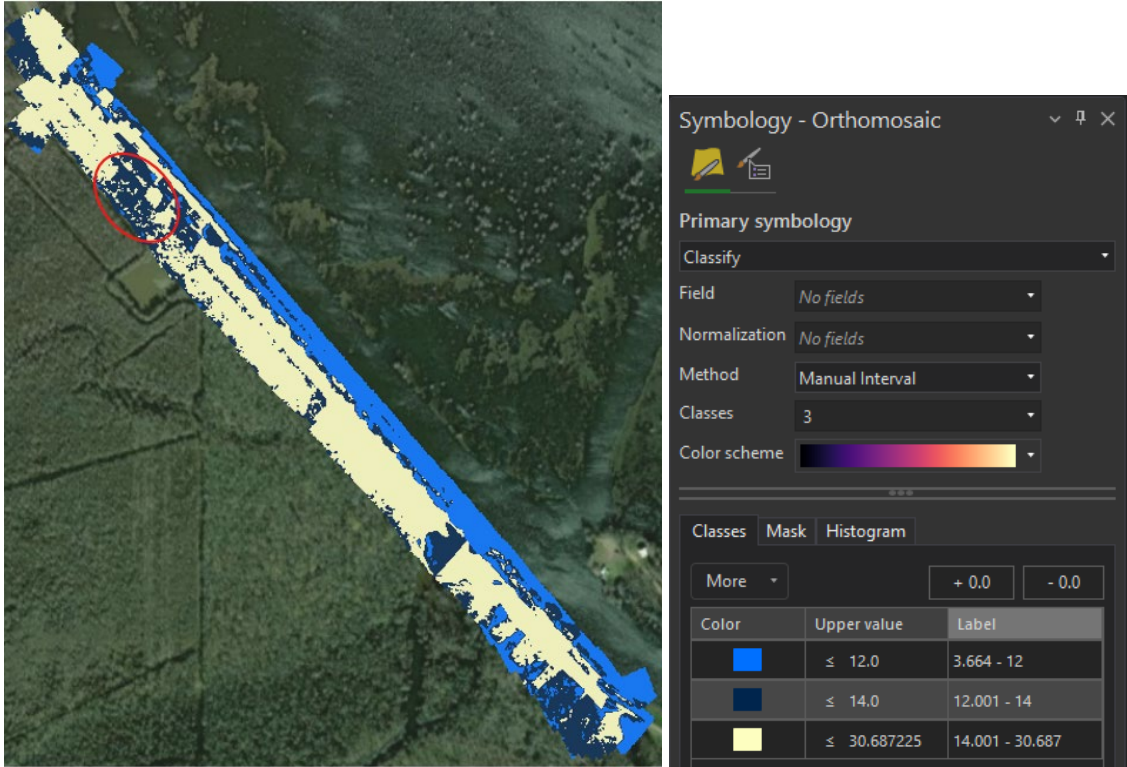


(e) RedEdge Band

Figure 64. Thermal map for Iatt Lake Dam



(a) Classify with six classes



(b) Classify with three classes

Figure 65. Sliding area for Iatt Lake Dam



(a) Front View

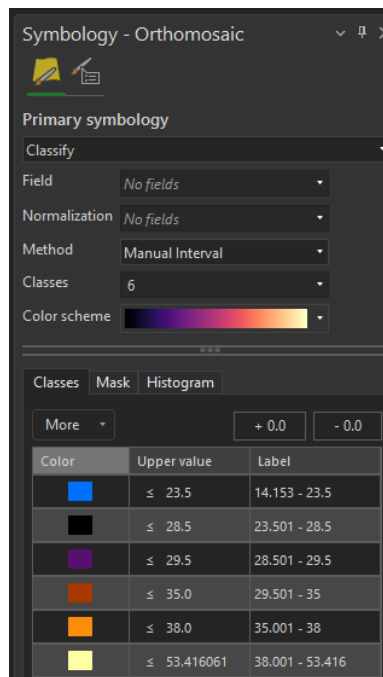


(b) Side View

Field Testing at Vernon Lake Dam Site

As shown earlier, using only the multispectral RedEdge camera to distinguish different moisture zones was not successful in this study and we do not have the capability of creating TVDI map. Additionally, the available batteries only allow the drone to fly less than an hour. Considering all these factors, only a thermal camera was brought to the Vernon Lake dam for capturing imaging data on April 21, 2022. It was a cloudy day with the temperature of 88°F (31°C). The flight height was 200 ft. Figure 66 shows the thermal map created with Drone2Map 2022.1 version using “classify” symbology with the number of classes being six or less. (in black/dark blue color). Since open water of the Vernon Lake was captured in images and was much cooler than the land surface, a separate class was created for the water body only. A couple of low thermal reading areas stand out in the images. Ground visual inspection identified a seepage area located in low thermal reading areas as shown in Figure 66d and e. An area that had a seepage issue before, according to dam safety engineer, also showed low thermal readings but to a lesser extent. The grass in this area was very tall and the detailed ground inspection was not conducted at that time due to safety concern (snakes). The results here showed that the drone-mounted thermal camera can provide initial information of difficult access areas and identify potential problematic areas in highway embankment and dam inspections. Therefore, it can be used as a labor, time, and cost-saving tool to supplement the information available to inspectors and dam owners.

Figure 66. Thermal map for Vernon Lake Dam



(a) Classify with 6 classes



Symbology - Orthomosaic

Primary symbology

Classify

Field: No fields

Normalization: No fields

Method: Manual Interval

Classes: 3

Color scheme: [Color gradient]

Classes | Mask | Histogram

More +0.0 -0.0

Color	Upper value	Label
[Blue]	≤ 23.5	14,153 - 23,5
[Dark Blue]	≤ 29.5	23,501 - 29,5
[Yellow]	≤ 53.416061	29,501 - 53,416

(b) Classify with 3 classes

Conclusions

Based on the testing results of laboratory and field studies on soil moisture content detection using thermal camera and multispectral camera, the following conclusions can be drawn:

- The study demonstrated promising results in using drone-mounted thermal camera to qualitatively distinguish different moisture zones. This capability is sufficient for identifying potential problematic areas in highway embankment and dam inspections. However, further research will be needed to use infrared thermography technology for quantitative determination of soil moisture content. The drone-based infrared thermography technology cannot replace the expertise of an experienced inspector in its current state, but it can serve as an effective tool for rapidly mapping highway embankments and dam slopes surface moisture conditions with full coverage of inspected sites.
- A multispectral camera alone was not effective to distinguish different moisture zones with the soil moisture estimation methods explored in this study.
- The index combining land surface temperature and vegetation within the NDVI/LST space showed promising results. However, due to limited resources available to the researchers in this study, this approach was not fully explored.
- This research primarily focused on the spatial variation of moisture-dependent land surface temperature to assess the condition of a highway embankments and dams. The study did not explore the variation of soil moisture content over time in an embankment or dam, which has more practical implications, and should be investigated in future studies.
- Image processing and analytical tools are necessary for constructing maps and processing the data (i.e., image data extraction, categorization, and interpretation) with the characteristics of real-time analytics and reporting, high accuracy, and user friendly.
- Only a limited number of electromagnetic spectral bands were investigated in this research. Soil moisture content may be more sensitive to other spectral bands which were not investigated in this study, e.g., SWIR.

Recommendations

- DOTD engineers explore and adopt market-available drone-based infrared thermography technology in routine highway embankment and dam inspections to supplement traditional ground inspections.
- Future research can explore more electromagnetic spectral bands to find the band or combination of bands that is most sensitive to the combined effects of soil and moisture. Hyperspectral imagery could be a suitable option for this.
- Various techniques of combining land surface temperature and vegetation mapping within vegetation index/temperature (VIT) space should be explored considering that vegetation is very common in soil embankments and dams.
- Future research on spatiotemporal variation of moisture-dependent land surface temperature is recommended to better monitor the risk of stability failure of the embankments/dams.
- Additional research is recommended to explore the use of infrared thermography for quantitative determination of the soil moisture content.
- Future researchers are advised to work together with software developers to develop an image processing and analytical tool specifically designed for highway embankment and dam inspections.

Acronyms, Abbreviations, and Symbols

Term	Description
AASHTO	American Association of State Highway and Transportation Officials
ATI	apparent thermal inertia
cm	centimeter
CRP	calibrated reflectance panel
CWSI	crop water stress index
DN	Digital Number
DOTD	Louisiana Department of Transportation and Development
EWT	equivalent water thickness
FHWA	Federal Highway Administration
ft.	foot (feet)
FWHM	full width at half maximum
GHz	Gigahertz
GNDVI	Green Normalized Difference Vegetation Index
GOM	geometrical optical model
HFOV	horizontal field of view
Hz	Hertz
IEM	integral equation model
in.	inch(es)
lb.	pound(s)
LST	land surface temperature
LTRC	Louisiana Transportation Research Center
LWIR	long-wave infrared
mm	millimeter
MHz	Megahertz
MIMICS	Michigan Microwave Canopy Scattering model
MWIR	mid-wave infrared
NDVI	Normalized Difference Vegetation Index
NDWI	Normalized Difference Water Index

Term	Description
NINSOL	Normalized Index of N_{SWIR} domain for Soil Moisture estimation from Linear correlation
NINSON	Normalized Index of N_{SWIR} domain for Soil moisture content estimation from Nonlinear correlation
NIR	near infrared
nm	nanometer
NSMI	Normalized Soil Moisture Index
POM	physical optic model
PRF	Pavement Research Facility
RH	relative humidity
SPM	small perturbation model
sUAS	small Unmanned Aircraft System
SWIR	shortwave infrared
THz	Terahertz
TVDI	temperature vegetation dryness index
UHF	Ultra high frequency
USCS	Unified Soil Classification System
VCI	Vegetation Condition Index
VFOV	Vertical field of view
VIT	vegetation index/temperature
WDI	water deficit index
WISOIL	Water Index SOIL
μm	micrometer

References

- [1] Z. Zhang, M. Tao and M. Morvant, "Cohesive Slope Surface Failure and Evaluation," *Journal of Geotechnical and Geoenvironmental Engineering*, vol. 131, no. 7, p. 898–906, May 2005.
- [2] G. Gregory, "Mechanism of Shallow Slope Failures in Clay," in *ASCE Texas Section Fall Meeting, Geotechnical Section*, Dallas, 1998.
- [3] G. H. Gregory and D. Chill, "Stabilization of Earth Slopes with Fiber Reinforcement," in *Proc., 6th int. Conf. On Geosynthetics, International Geosynthetics Society*, Atlanta, 1998.
- [4] L. O. o. S. Climatology, "December 2002 Newsletter," December 2002. [Online]. Available: https://www.losc.lsu.edu/products/monthly/dec_2002.pdf. [Accessed 10 April 2023].
- [5] J. Eagleman and W. Lin, "Remote Sensing of Soil Moisture by a 21 cm Passive Radiometer," *Journal of Geophysical Research*, vol. 81, pp. 3660-3666, 1976.
- [6] A. Patel, "Studies on Variation of Spectral Signatures in Relation to Certain Geotechnical Properties of Soil Samples," Ph.D. Thesis, University of Indore, Indore, India, 1979.
- [7] T. Schmugge, T. Gloersen, T. Wilheit and F. Geiger, "Remote Sensing of Soil Moisture with Microwave Radiometers," *Journal of Geophysical Research*, vol. 79, pp. 317-323, 1974.
- [8] F. Ulaby, "Radar Measurement of Soil Moisture Content," *IEEE Transactions on Antennas and Propagation*, vol. 22, pp. 257-265, 1974.
- [9] J. Yue, J. Tian, Q. Tian, K. Xu and N. Xu, "Development of soil moisture indices from differences in water absorption between shortwave-infrared bands," *ISPRS Journal of Photogrammetry and Remote Sensing*, vol. 154, pp. 216-230, 2019.

- [10] E. a. M. National Academies of Sciences, Handbook of Frequency Allocations and Spectrum Protection for Scientific Uses: Second Edition, Washington, DC: The National Academies Press, 2015.
- [11] J. Wang, "Effect of Vegetation on Soil Moisture Sensing Observed from Orbiting Microwave Radiometers," *Remote Sensing of Environment*, vol. 17, pp. 141-151, 1985.
- [12] E. Njoku and I. Patel, "Observations of the Seasonal Variability of Soil Moisture and Vegetation Cover over Africa Using Satellite Microwave Radiometry," in *ESA Proceedings of an International Satellite Land-Surface Climatology Project (ISLSCP) Conferenc*, Rome, Italy, 1986.
- [13] T. Jackson, A. Gasiewski, A. Oldak, M. Klein, E. Njoku, A. Yevgrafov, S. Christiani and R. Bindlish, "Soil Moisture Retrieval Using the C-Band Polarimetric Scanning Radiometer During the Southern Great Plains 1999 Experiments," *IEEE Transactions on Geoscience and Remote Sensing*, vol. 40, pp. 2151-2161, 2002.
- [14] T. Jackson, T. Schmugge and J. Wang, "Passive Microwave Remote Sensing of Soil Moisture under Vegetation Canopies," *Water Resources Research*, vol. 18, pp. 1137-1142, 1982.
- [15] J. Wigneron, M. Parde, P. Waldteufel, A. Chanzy, Y. Kerr, S. Schmidl and N. Skou, "Characterizing the Dependence of Vegetation Model Parameters on Crop Structure, Incidence Angle, and Polarization at L-Band," *IEEE Transactions on Geoscience and Remote Sensing*, vol. 42, pp. 416-425, 2004.
- [16] M. Schwank, C. Matzler, M. Guglielmetti and H. Fluhler, "L-Band Radiometer Measurements of Soil Water Under Growing Clover Grass," *IEEE Transactions on Geoscience and Remote Sensing*, vol. 43, pp. 2225-2237, 2005.
- [17] L. Dente, "Microwaving Remote Sensing for Soil Moisture Monitoring: Synergy of Active and Passive Observations and Validation of Retrieved Products," University of Twente, Cerignola, Italy, 2016.

- [18] Z. Gao, X. Xu, J. Wang, H. Yang, W. Huang and H. Feng, "A Method of Estimating Soil Moisture Based on the Linear Decomposition of Mixture Pixels," *Mathematical and Computer Modeling*, vol. 58, no. 3-4, pp. 606-613, 2013.
- [19] J. R. Wang, E. T. Engmen, J. C. Shiue, M. Rusek and C. Steinmeier, "The SIR-B Observations of Microwave Backscatter Dependence on Soil Moisture, Surface Roughness, and Vegetation Covers," *IEEE Transactions on Geoscience and Remote Sensing*, Vols. GE-24, no. 4, pp. 510-516, 1986.
- [20] Y. Wu, J. Bao, Z. Liu, Y. Bao and G. P. Petropoulos, "Investigation of the Sensitivity of Microwave Land Surface Emissivity to Soil Texture in MLEM," *Remote Sensing*, vol. 14, no. 13, p. <https://doi.org/10.3390/rs14133045>, 2022.
- [21] N. Chauhan, "Soil Moisture Estimation Under a Vegetation Cover: Combined Active Passive MICrowave Remote Sensing Approach," *International Journal of Remote Sensing*, vol. 18, pp. 1079-1097, 1997.
- [22] Y. Liu, W. Dorigo, R. Parinussa, R. De Jeu, W. Wagner, M. McCabe, J. Evans and A. van Dijk, "Trend-preserving blending of passive and active microwave soil moisture retrievals," *Remote Sensing of Environment*, vol. 123, pp. 280-297, 2012.
- [23] P. O'Neill, N. Chauhan and T. Jackson, "Use of Active and Passive Microwave Remote Sensing for Soil Moisture Estimation Through Corn," *International of Journal of Remote Sensing*, vol. 17, pp. 1851-1865, 1996.
- [24] S. Saatchi, E. Njoku and U. Wegmuller, "Synergism of Active and Passive Microwave Data for Estimating Bare Soil Surface Moisture," in *Passive Microwave Remote Sensing of Land-Atmosphere Interactions*, Saint Lary, France, 1995.
- [25] S. Theis, A. Blanchard and B. Blanchard, "Utilization of Active Microwave Roughness Measurements to Improve Passive Microwave Soil Moisture Estimates over Bare Soils," *IEEE Transactions on Geoscience and Remote Sensing*, Vols. GE-24, pp. 334-339, 1986.
- [26] J. Wen, Z. Su and Y. Ma, "Determination of Land Surface Temperature and Soil Moisture from Tropical Rainfall Measuring Mission/Microwave Imager Remote

- Sensing Data," *Journal of Geophysical Research-Atmospheres*, vol. 18, no. D2, pp. ACL 2-1-ACL 2-10, 2003.
- [27] X. Zhan, P. Houser, J. Walker and W. Crow, "A Method for Retrieving High-Resolution Surface Soil Moisture from Hydros L-Band Radiometer and Radar Observations," *IEEE Transactions on Geoscience and Remote Sensing*, vol. 44, pp. 1534-1544, 2006.
- [28] D. Matsushima, "Thermal Inertia-Based Method for Estimating Soil Moisture," in *Soil Moisture*, IntechOpen, 2018.
- [29] R. Jackson, S. Idso and R. Reginato, "Canopy Temperature As A Crop Water Stress Indicator," *Water Resource Research*, vol. 17, no. 1, pp. 133-138, 1981.
- [30] S. Lu, Z. Ju, T. Ren and R. Horton, "A General Approach to Estimate Soil Water Content from Thermal Inertia," *Agricultural and Forest Meteorology*, vol. 149, pp. 1693-1698, 2009.
- [31] Y. Lu, R. Horton, X. Zhang and T. Ren, "Accounting for Soil Porosity Improves a Thermal Inertia Mode for Estimating Surface Soil Water Content," *Remote Sensing of Environment*, vol. 212, pp. 79-89, 2018.
- [32] A. Maltese, P. Bates, F. Capodici, M. Cannarozzo, G. Ciraolo and G. La Loggia, "Critical Analysis of Thermal Inertia Approaches for Surface Soil Water Content Retrieval," *Hydrological Sciences Journal*, vol. 58, pp. 1144-1161, 2013.
- [33] D. Matsushima, R. Kimura and M. Shinoda, "Soil Moisture Estimation Using Thermal Inertia: Potential and Sensitivity to Data Conditions," *Journal of Hydrometeorology*, vol. 13, pp. 638-648, 2012.
- [34] M. Minacapilli, C. Cammalleri, G. Ciraolo, F. D'Asaro, M. Iovino and A. Maltese, "Thermal Inertia Modeling for Soil Surface Water Content Estimation: A Laboratory Experiment," *Soil Science Society of America Journal*, vol. 76, pp. 92-100, 2012.

- [35] M. Minacapilli, M. Iovino and F. Blanda, "High Resolution Remote Estimation of Soil Surface Water Content by A thermal Inertia Approach," *Journal of Hydrology*, vol. 379, pp. 229-238, 2009.
- [36] J. Vlcek and D. King, "Detection of Subsurface Soil Moisture by Thermal Sensing: Results of Laboratory, Close-Range, and Aerial Studies," *Photogrammetric Engineering and Remote Sensing*, vol. 49, no. 11, pp. 1593-1597, 1983.
- [37] G. Pegram, "Soil Moisture from Satellites: Daily Maps Over RSA," WRC Report No. K5/1683, South Africa, 2006.
- [38] D. Matsushima, "Estimating Regional Distribution of Surface Heat Fluxes by Combining Satellite Data and A Heat Budget Model Over the Kherlen River Basin, Mongolia," *Journal of Hydrology*, vol. 333, pp. 86-99, 2007.
- [39] A. Maltese, M. Minacapilli, C. Cammalleri, G. Ciraolo and F. D'Asaro, "A Thermal Inertia Model for Soil Water Content Retrieval Using Thermal and Multispectral Images," in *Proceedings of SPIE Vol. 7824*, 2010.
- [40] M. Mario, C. Cammalleri, G. Ciraolo, F. D'Asaro, M. Iovino and A. Maltese, "Thermal Inertia Modeling for Soil Surface Water Content Estimation: A Laboratory Experiment," *Soil Science Society of America Journal*, vol. 76, no. 1, pp. 92-100, 2012.
- [41] M. Moran, T. Clarke, W. Kustas, M. Weltz and S. Amer, "Evaluation of Hydrologic Parameters in A Semiarid Rangeland Using Remotely Sensed Spectral Data," *Water Resources Research*, vol. 30, no. 5, pp. 1287-1297, 1994.
- [42] P. Colaizzi, C. Choi, P. Waller, E. Barnes and T. Clarke, "Determining Irrigation Management Zones in Precision Agriculture Using the Water Deficit Index at High Spatial Resolutions," in *ASAE Annual International Meeting, Technical Papers: Engineering Solution for A New Century*, Milwaukee, WI, 2000.
- [43] I. Sandholt, K. Rasmussen and J. Andersen, "A Simple Interpretation of the Surface Temperature/Vegetation Index Space for Assessment of Surface Moisture Status," *Remote Sensing of Environment*, vol. 79, no. 2-3, pp. 213-224, 2002.

- [44] L. Yuan, L. Li, T. Zhang, L. Chen, J. Zhao, S. Hu, L. Cheng and W. Liu, "Soil Moisture Estimation for the Chinese Loess Plateau Using MODIS Derived ATI and TVDI," *Remote Sensing*, vol. 12, no. 18, 2020.
- [45] E. Mira, E. Valor, R. Boluda, V. Caselles and C. Coll, "Influence of Soil Water Content on the Thermal Infrared Emissivity of Bare Soils: Implication for Land Surface Temperature Determination," *Journal of Geophysical Research*, vol. 112, no. F04003, 2007.
- [46] J. Chen, B. Yang and R. Zhang, "Soil Thermal Emissivity As Affected by Its Water Content and Surface Treatment," *Soil Science*, vol. 148, no. 6, pp. 433-435, 1989.
- [47] M. Mira, E. Valor, V. Caselles, E. Rubio, C. Coll, J. M. Galve, R. Niclos, J. M. Sanchez and R. Boluda, "Soil Moisture Effect on Thermal Infrared (8-13-um) Emissivity," *IEEE Transactions on Geoscience and Remote Sensing*, vol. 48, no. 5, pp. 2251-2260, 2010.
- [48] J. W. Salisbury and D. M. D'Aria, "Emissivity of Terrestrial Materials in the 8-14 um Atmospheric Window," *Remote Sensing of Environment*, vol. 42, pp. 83-106, 1992.
- [49] J. M. Sanchez, A. N. French, M. Mira, D. J. Hunsaker, K. R. Thorp, E. Valor and V. Caselles, "Thermal Infrared Emissivity Dependence on Soil Moisture in Field Conditions," *IEEE Transactions on Geoscience and Remote Sensing*, vol. 49, no. 11, pp. 4652-4659, 2011.
- [50] O. Ogawa, T. Schmugge and S. Rokugawa, "Observations of the Dependence of the Thermal Infrared Emissivity on Soil Moisture," *Geophysical Research Abstracts*, vol. 8, no. 04996, 2006.
- [51] C. Van Bavel and D. Hillel, "Calculating Potential and Actual Evaporation from A Bare Soil Surface by Simulation of Concurrent Flow of Water and Heat," *Agricultural Meteorology*, vol. 17, pp. 453-476, 1976.
- [52] E. Rubio, V. Caselles and C. Badenas, "Emissivity Measurements of Several Soils and Vegetation Types in the 8-14 um Wave Band: Analysis of Two Field Methods," *Remote Sensing of Environment*, vol. 59, pp. 490-521, 1997.

- [53] E. Rubio, V. Caselles, C. Coll, E. Valour and F. Sospedra, "Thermal–infrared emissivities of natural surfaces: improvements on the experimental set-up and new measurements," *International Journal of Remote Sensing*, vol. 24, no. 24, pp. 5379-5390, 2003.
- [54] S. Fabre, X. Briottet and A. Lesaignoux, "Estimation of Soil Moisture Content from the Spectral Reflectance of Bare Soils in the 0.4-2.5 um Domain," *Sensors*, vol. 15, pp. 3262-3281, 2015.
- [55] D. Neema, A. Shah and A. Patel, "A Statistical Optical Model for Light Reflection and Penetration through Sand," *International Journal of Remote Sensing*, vol. 8, pp. 1209-1217, 1987.
- [56] D. Lobell and G. Asner, "Moisture Effects on Soil Reflectance," *Soil Science Society of America Journal*, vol. 66, no. 3, pp. 722-727, 2002.
- [57] E. Muller and H. Décamps, "Modeling soil moisture–reflectance," *Remote Sensing of Environment*, vol. 76, no. 2, pp. 173-180, 2001.
- [58] Q. Qin, Z. Wu, T. Zhang, V. Sagan, Z. Zhang, Y. Zhang, C. Zhang, H. Ren, Y. Sun, W. Xu and C. Zhao, "Optical and Thermal Remote Sensing for Monitoring Agricultural Drought," *Remote Sensing*, vol. 13, no. 5092, 2021.
- [59] J. Féret, A. Gitelson, S. Noble and S. Jacquemoud, "PROSPECT-D: Towards Modeling Leaf Optical Properties through A Complete Lifecycle," *Remote Sensing of Environment*, vol. 193, pp. 204-215, 2017.
- [60] A. J. Peters, E. Walter-Shea, Ji, L., A. Viña, M. J. Hayes and M. Svoboda, "Drought monitoring with NDVI-based Standardized Vegetation Index," *Photogrammetric Engineering and Remote Sensing*, vol. 68, no. 1, pp. 71-75, 2002.
- [61] S. Haubrock, S. Chabrillat, C. Lemnitz and H. Kaufmann, "Surface Soil Moisture Quantification Models from Reflectance Data under Field Condition," *International Journal of Remote Sensing*, vol. 29, pp. 3-29, 2008.

- [62] W. Whalley, P. Leeds-Harrison and G. Bowman, "Estimation of Soil Moisture Status Using Near Infrared Reflectance," *Hydrological Processes*, vol. 5, pp. 321-327, 1991.
- [63] W. Liu, F. Baret, X. Gu, Q. Tong, L. Zheng and B. Zhang, "Relating Soil Surface Moisture to Reflectance," *Remote Sensing Environment*, vol. 81, pp. 238-246, 2002.
- [64] B. Gao, "NDWI-A Normalized Difference Water Index for Remote Sensing of Vegetation Liquid Water from Space," *Remote Sensing Environment*, vol. 58, pp. 257-266, 1996.
- [65] R. Fensholt and I. Sandholt, "Derivation of a shortwave infrared water stress index from MODIS near- and shortwave infrared data in a semiarid environment," *Remote Sensing of Environment*, vol. 87, no. 1, pp. 111-121, 2003.
- [66] S. McFeeters, "The Use of the Normalized Difference Water Index (NDWI) in the Delineation of Open Water Features," *International Journal of Remote Sensing*, vol. 17, pp. 1425-1432, 1996.
- [67] A. K. Taloor, D. S. Manhas and G. C. Kothyari, "Retrieval of land surface temperature, normalized difference moisture index, normalized difference water index of the Ravi basin using Landsat data," *Applied Computing and Geosciences*, vol. 9, 2021.
- [68] F. N. Kogan, "Remote sensing of weather impacts on vegetation in non-homogeneous areas," *International Journal of Remote Sensing*, vol. 11, no. 8, pp. 1405-1419, 1990.
- [69] V. Mishra, J. F. Cruise, C. R. Hain, J. R. Mecikalski and M. C. Anderson, "Development of soil moisture profiles through coupled microwave-thermal infrared observations in the southeastern United States," *Hydrology and Earth System Sciences*, vol. 22, no. 9, pp. 4935-4957, 2018.
- [70] S. Hasan, C. Montzka, C. Rüdiger, M. Ali, H. R. Bogen and H. Vereecken, "Soil moisture retrieval from airborne L-band passive microwave using high resolution multispectral data," *ISPRS Journal of Photogrammetry and Remote Sensing*, vol. 91, pp. 59-71, 2014.

- [71] P. Rahimzadeh-Bajgiran, A. A. Berg, C. Champagne and K. Omasa, "Estimation of soil moisture using optical/thermal infrared remote sensing in the Canadian Prairies," *ISPRS Journal of Photogrammetry and Remote Sensing*, vol. 83, pp. 94-103, 2013.
- [72] J. Wang, Z. Ling, Y. Wang and H. Zeng, "Improving spatial representation of soil moisture by integration of microwave observations and the temperature–vegetation–drought index derived from MODIS products," *ISPRS Journal of Photogrammetry and Remote Sensing*, vol. 113, pp. 144-154, 2016.